# Methane retrieval from airborne HySpex observations in the short-wave infrared

Philipp Hochstaffl[1], Franz Schreier[1], Claas Henning Köhler[1], Andreas Baumgartner[1], and Daniele Cerra[1]

[1]Deutsches Zentrum für Luft- und Raumfahrt, Institut für Methodik der Fernerkundung, 82234 Oberpfaffenhofen, Germany

**Correspondence:** Philipp Hochstaffl (philipp.hochstaffl@dlr.de)

**Abstract.** A reduction of methane emissions could help to mitigate global warming on a relatively short time scale. Monitoring of local and regional anthropogenic $CH_4$ emissions is crucial in order to increase our understanding of the methane budget which is still subject to scientific debate.

The study compares various retrieval schemes that estimate localized $CH_4$ emissions from ventilation shafts in the Upper Silesian Coal Basin (USCB) in Poland using short-wave infrared nadir observations of the airborne imaging spectrometer HySpex. The examined methods are divided into nonlinear and linear schemes. The former class are of iterative nature and encompass various nonlinear least squares setups while the latter are represented by the Matched Filter (MF), Singular Value Decomposition (SVD) and Spectral Signature Detection (SSD) algorithms. Particular emphasis is put on strategies to remedy the problem of albedo related biases due to correlation with broad band absorption features caused by the hyperspectral instrument's low spectral resolution.

It was found that classical nonlinear least squares fits based on the Beer InfraRed Retrieval Algorithm (BIRRA) suffers from surface-type dependent biases. The effect is more pronounced for retrievals from single spectral intervals but can be mitigated when multiple intervals are combined. The albedo related correlation is also found in the BIRRA solutions for the separable least squares. A new BIRRA setup that exploits the inverse of a scene's covariance structure to account for reflectivity statistics significantly reduces the albedo bias and enhances the $CH_4$ signal so that the method infers two- to threefold higher methane concentrations.

The linear estimators turned out to be very fast and well suited to detect enhanced levels of methane. The linearized BIRRA forward model turned out to be sensitive to the selected retrieval interval and in the default setup only works for very narrow windows. Other well established linear methods such as the MF and SVD identified the methane pattern as well and largely agree with the BIRRA fitted enhancements hence the methods allow quantitative estimates of methane. The latter two methods yielded increased performance when the scene was further divided into clusters by applying k-means in a preprocessing step. Methane plumes detected with the simple SSD method were faint and found rather sensitive to the polynomial used to compute the method's residuum ratio.

---

(Revised version)

# Methane retrieval from airborne HySpex observations in the short-wave infrared

Philipp Hochstaffl[1], Franz Schreier[1], Claas Henning Köhler[1], Andreas Baumgartner[1], and Daniele Cerra[1]

[1]Deutsches Zentrum für Luft- und Raumfahrt, Institut für Methodik der Fernerkundung, 82234 Oberpfaffenhofen, Germany

**Correspondence:** Philipp Hochstaffl (philipp.hochstaffl@dlr.de)

**Abstract.** A reduction of methane emissions could help mitigate global warming on a short time scale, making monitoring of local and regional anthropogenic methane emissions crucial for understanding the methane budget. The study compares various retrieval schemes for estimating localized methane enhancements around ventilation shafts in the Upper Silesian Coal Basin in Poland, using nadir observations in the short-wave infrared from the airborne imaging spectrometer HySpex. Nonlinear and linear methods are examined and put into perspective, with an emphasis on strategies to address degeneracies between the surface reflectivity and the broad band molecular absorption features attributed to the instrument's low spectral resolution. The results demonstrate that the weighted nonlinear least squares fit in the Beer InfraRed Retrieval Algorithm (BIRRA), where the scene's background covariance structure accounts for the reflectivity statistics, is able to quantify enhanced methane levels from hyperspectral data with good accuracy and precision. Some BIRRA setups suffer from surface-type dependent biases although combining multiple spectral intervals mitigates the adverse impact. Linear estimators such as the Matched Filter (MF) and the Singular Value Decomposition (SVD) are fast and able to detect and to a certain extend quantify enhanced levels of methane. Using k-means clustering in a preprocessing step can further enhance the performance of the two linear solvers. The linearized BIRRA fit (LLS) underestimates methane but agrees well on the enhancement pattern. The non-quantitative Spectral Signature Detection (SSD) method does not require any forward modeling and can be useful in the detection of relevant scenes. In conclusion, the BIRRA code — originally designed for the retrieval of atmospheric constituents from space borne high resolution spectra, turned out to be applicable to hyperspectral imaging data for the quantification of methane plumes from point-like sources. Moreover, it is able to outperform well established linear schemes such as the MF or SVD, however, at the expense of high(er) computing time.

## 1 Introduction

Methane ($CH_4$) is the second most important anthropogenic greenhouse gas next to carbon dioxide ($CO_2$) according to the latest IPCC report (Masson-Delmotte et al., 2021). Due to its comparatively short lifetime of approximately 9 years, a reduction of methane emissions could help to mitigate global warming on a relatively short time scale of approximately one decade. Despite improvements in monitoring regional and global $CH_4$ emissions in recent years the IPCC report points out that fundamental uncertainties pertaining to the methane budget remain (Intergovernmental Panel on Climate Change, 2014).

## 1 Introduction

25 Methane ($CH_4$) is the second most important greenhouse gas next to carbon dioxide ($CO_2$) according to the latest IPCC report (Masson-Delmotte et al., 2021). Due to its comparatively short lifetime of approximately 9 years, a reduction of methane emissions could help to mitigate global warming on a relatively short time scale of approximately one decade. Despite improvements in monitoring regional and global $CH_4$ emissions in recent years the IPCC report points out that fundamental uncertainties pertaining to the methane budget remain (Intergovernmental Panel on Climate Change, 2014).

30 Observations indicate an increasing trend in atmospheric $CH_4$ content since 2007, the cause of which is still subject to scientific debate. The vast majority of anthropogenic $CH_4$ emissions is caused by small scale phenomena such as agriculture (enteric fermentation & manure), waste management (landfills) and fossil fuel exploitation, where the latter is responsible for 20-30 % of all anthropogenic $CH_4$ emissions. Consequently there exists the need for continuous long-term methane observations on a global scale, in order to foster understanding on the global methane cycle, devise future reduction measures and

35 monitor their effectiveness. The monitoring of anthropogenic emissions of $CH_4$ and $CO_2$ is also part of the United Nations Framework Convention on Climate (2015) as nationally determined contributions should be assessed via global stock takes on a 5 year basis from 2023 (Article 13 & 14 of the Paris Agreement).

Satellite observations are typically the method of choice for such continuous and global long-term observations. Space-borne spectrometers measuring short-wave infrared (SWIR) solar radiation reflected at the Earth surface are especially well suited to

40 observe atmospheric $CH_4$ in the lower atmosphere by measuring its absorption in the bands 1560-1660 nm and 2090-2290 nm. In contrast, the thermal infrared is less sensitive to variations in $CH_4$ concentration close to the surface. Moreover, thermal sensors often have lower spatial resolution making them less favorable for emission monitoring (Richter, 2010).

Operational $CH_4$ products from contemporary atmospheric composition missions such as TROPOMI (TROPOspheric Monitoring Instrument; Veefkind et al. (2012)), GOSAT/GOSAT-2 (Greenhouse gases Observing SATellite; Kuze et al. (2009, 2016))

45 measure trace gas concentrations with very high accuracy, nevertheless, they are not optimally suited to measure emissions of point-like sources. This design inherent limitation is due to their focus on rapid global coverage, which entails a comparatively coarse spatial resolution of several square kilometers per pixel. Since the emission of a single point source inside a pixel is averaged over the entire resolution cell, even large sources seldomly elevate the mean $CH_4$ concentration within one pixel by more than one percent compared to the undisturbed background (Lauvaux et al., 2022). A way to increase the contrast

50 of enhancements is to operate typical atmospheric remote sensing spectrometers at lower altitudes (e.g. on aircraft), thus increasing the spatial resolution while leaving the overall optical design untouched. This strategy is followed by instruments such as MAMAP/MAMAP-2D (Gerilowski et al., 2011) or GHOST (Humpage et al., 2018) which are very well suited for the calibration and validation of their space-borne counterparts.

In order to increase the sensitivity towards smaller sources an increased spatial resolution is required, which in turn ne-

55 cessitates a trade-off in spectral resolution because the loss of photons caused by the smaller emitting area per pixel reduces the Signal-to-Noise Ratio (SNR) of the image which has to be compensated by broadening the spectral interval per spectral channel. Imaging spectrometers for land surface remote sensing (often referred to as hyperspectral cameras) are typical exam-

---

25 Observations indicate an increasing trend in atmospheric $CH_4$ content since 2007, the cause of which is still subject to scientific debate. The vast majority of anthropogenic $CH_4$ emissions is caused by small scale phenomena such as agriculture (enteric fermentation & manure), waste management (landfills) and fossil fuel exploitation, where the latter is responsible for 20-30 % of all anthropogenic $CH_4$ emissions. Consequently there exists the need for continuous long-term methane observations on a global scale, in order to foster understanding on the global methane cycle, devise future reduction measures and

30 monitor their effectiveness. The monitoring of anthropogenic emissions of $CH_4$ and $CO_2$ is also part of the United Nations Framework Convention on Climate (2015) as nationally determined contributions should be assessed via global stock takes on a 5 year basis from 2023 (Article 13 & 14 of the Paris Agreement).

Satellite observations are typically the method of choice for such continuous and global long-term observations although also ground based networks such as the Global Atmosphere Watch (GAW) Programme of the World Meteorological Organ-

35 isation (WMO) or the European Integrated Carbon Observation System (ICOS) are crucial assets in monitoring atmospheric composition. Space-borne spectrometers measuring short-wave infrared (SWIR) solar radiation reflected at the Earth surface are especially well-suited to observe atmospheric $CH_4$ in the lower atmosphere by measuring its absorption around 1.6 $\mu$m and and 2.3 $\mu$m. In contrast, the thermal infrared is less sensitive to variations in $CH_4$ concentration close to the surface. Moreover, mid-infrared sensors often have lower spatial resolution making them less favorable for emission monitoring (Richter, 2010).

40 Operational $CH_4$ products from contemporary atmospheric composition missions such as TROPOMI (TROPOspheric Monitoring Instrument; Veefkind et al. (2012)), GOSAT/GOSAT-2 (Greenhouse gases Observing SATellite; Kuze et al. (2009, 2016)) measure trace gas concentrations with very high accuracy, nevertheless, they are not optimally suited to measure emissions of point-like sources. This design inherent limitation is due to their focus on rapid global coverage, which entails a comparatively coarse spatial resolution of several square kilometers per pixel. Since the emission of a single point source inside a pixel is

45 averaged over the entire resolution cell, even large sources seldomly elevate the mean $CH_4$ concentration within one pixel by more than one percent compared to the undisturbed background (Lauvaux et al., 2022). A way to increase the contrast of enhancements is to operate typical atmospheric remote sensing spectrometers at lower altitudes (e.g. on aircraft), thus increasing the spatial resolution while leaving the overall optical design untouched. This strategy is followed by instruments such as MAMAP/MAMAP-2D (Gerilowski et al., 2011) or GHOST (Humpage et al., 2018) which are very well-suited for the

50 calibration and validation of their space-borne counterparts.

In order to increase the sensitivity towards smaller sources an increased spatial resolution is required. This in turn necessitates a trade-off in spectral resolution because the loss of photons caused by the smaller ground pixels reduces the Signal-to-Noise Ratio (SNR) of the image which has to be compensated by broadening the spectral interval per spectral channel. Imaging spectrometers for land surface remote sensing (often referred to as hyperspectral cameras) are typical examples of instruments

55 optimized for spatial resolution this way. Their technology matured over the last 30 years and a variety of airborne instruments and several space-borne versions are either in orbit Guanter et al. (2021, PRISMA), Chabrillat et al. (2020, ENMAP) or going to be launched in the future Rast et al. (2021, CHIME). Yet other sensors dedicated for the detection of methane Jervis et al. (2021, GHGSat) or MethaneSat and carbon dioxide, e. g., Hochstaffl et al. (2023, CO2Image), have slightly higher spectral

ples of instruments optimized for spatial resolution this way. Their technology matured over the last 30 years and a variety of airborne instruments and several space-borne versions are either in orbit (PRISMA, Guanter et al., 2021; ENMAP, Chabrillat et al., 2020) or going to be launched in the future (CHIME). Yet other sensors dedicated for the detection of methane (GHGSat, Jervis et al., 2021) and carbon dioxide (e. g., Carbon Mapper, CO2Image) have slightly higher spectral resolution than their hyperspectral counterparts but still offer a much higher spatial resolution than atmospheric composition missions.

Thorpe et al. (2013) were the first to demonstrate that localized $CH_4$ emissions over land can be detected from hyperspectral cameras with the Airborne Visible/Infrared Imaging Spectrometer (AVIRIS, Green et al. 1998) and that a limited quantitative analysis is possible (Thorpe et al., 2014). Similar studies were repeated with airborne instruments (AVIRIS-NG, Borchardt et al. 2021; HySpex, Nesme et al. 2020) and space-borne instruments (Thompson et al., 2016; Guanter et al., 2021). Works by Varon et al. (2019); Jervis et al. (2021) demonstrated that $CH_4$ sources can even be detected with the multi-spectral MSI instrument on-board the Sentinel-2 satellites, but these measurements are restricted to 'favourable conditions' (i. e., strong sources and high surface albedo).

One of the core challenges when retrieving methane from measurements with high spatial and moderate spectral resolution (> 1 nm) is the separation of spectral variations caused by molecular absorption and surface reflectivity. Classical trace gas retrievals for high-spectral resolution instruments such as RemoteC (Lorente et al., 2021), Weighting Function Modified Differential Optical Absorption Spectroscopy (WFM-DOAS, Buchwitz et al., 2005), or the Beer InfraRed Retrieval Algorithm (BIRRA, Gimeno García et al., 2011) exploit the high frequency characteristics of gaseous absorption and attribute the smooth varying part to the surface albedo. Instruments with coarse spectral resolution, however, are unable to sufficiently resolve those molecular signatures which causes ambiguities that often leads to surface-type related biases in the 'classical' retrieval schemes (e. g., Borchardt et al., 2021, Sec. 3.3 or Thorpe et al., 2014, Sec. 9.2). Alternative more 'data-driven' retrieval schemes such as the Matched Filter (MF) or the Singular Value Decomposition (SVD) estimate enhancements based on methods from linear algebra and statistics (Thorpe et al., 2013; Thompson et al., 2015; Thorpe et al., 2014).

This study compares various retrieval schemes applied to measurements from DLR's (German Aerospace Centre) HySpex sensor system and the paper is structured as follows. The next section briefly describes the experimental setup, provides a quick review of atmospheric radiation, and introduces the various BIRRA setups that were examined in this study. Thereafter, other (simpler but faster) retrieval schemes employed in this work are briefly described. The result section starts with a feasibility analysis for BIRRA with (simulated) HySpex data and proceeds with the presentation of the retrieval results from HySpex observations for different BIRRA setups over the Pniowek V ventilation shaft. Thereafter, the results from the well established 'data driven' fitting techniques such as MF and SVD, are presented. In the last chapter, results are sumarized and put into perspective.

## 2 Methodology

Methods introduced in this section can be divided into linear and nonlinear schemes. While the former are very fast and often of sufficient accuracy the nonlinear iterative solvers require more computing power and hence time to come up with a best

---

resolution than their hyperspectral counterparts but still offer a much higher spatial resolution than atmospheric composition missions.

Thorpe et al. (2013) were the first to demonstrate that localized $CH_4$ emissions over land can be detected from hyperspectral cameras with the Airborne Visible/Infrared Imaging Spectrometer Green et al. (1998, AVIRIS) and that a limited quantitative analysis is possible (Thorpe et al., 2014). Similar studies were repeated with airborne instruments (AVIRIS-NG, Frankenberg et al. 2016; Duren et al. 2019; Borchardt et al. 2021; HySpex, Nesme et al. 2020) and space-borne instruments (Thompson et al., 2016; Guanter et al., 2021). Varon et al. (2019) and Jervis et al. (2021) demonstrated that $CH_4$ sources can even be detected with the multi-spectral MSI instrument on-board the Sentinel-2 satellites, but these measurements are restricted to 'favourable conditions' (i. e., strong sources and high surface albedo).

One of the core challenges when retrieving methane from measurements with high spatial and moderate spectral resolution (> 1 nm) is the separation of spectral variations caused by molecular absorption and surface reflectivity (Ayasse et al., 2018). Classical trace gas retrievals for high-spectral resolution instruments such as RemoteC (Lorente et al., 2021), Weighting Function Modified Differential Optical Absorption Spectroscopy (Buchwitz et al., 2005, WFM-DOAS), or the Beer InfraRed Retrieval Algorithm (Gimeno García et al., 2011, BIRRA) exploit the high frequency characteristics of gaseous absorption and attribute the smooth varying part to the surface albedo and scattering. Instruments with coarse spectral resolution, however, are unable to sufficiently resolve those molecular signatures which causes ambiguities that often leads to surface-type related biases in the 'classical' retrieval schemes (e. g., Borchardt et al. (2021, Sec. 3.3) or Thorpe et al. (2014, Sec. 9.2)). Alternative more 'data-driven' retrieval schemes such as the Matched Filter (MF) or the Singular Value Decomposition (SVD) estimate enhancements based on methods from linear algebra and statistics (Thorpe et al., 2013; Thompson et al., 2015; Thorpe et al., 2014).

This study aims to compare various retrieval schemes applied to measurements from the German Aerospace Center's (DLR) HySpex sensor system. The objective is to evaluate the retrievals performance in terms of accuracy, precision and speed and show advantages and drawbacks for each method. Another goal is to assess the latest BIRRA updates and its applicability to moderately resolved spectra from airborne sensors. Therefore, the paper is structured as follows: First, the experimental setup is briefly described, followed by a quick review of atmospheric radiation and an introduction to the various BIRRA setups examined in this study. Afterward, other simpler but faster retrieval schemes employed in this work are briefly discussed. The result section starts with a feasibility analysis and then proceeds with the presentation of the retrieval results from HySpex observations over the Pniowek V ventilation shafts. In the last section, the results are summarized and put into perspective.

## 2 Methodology

The methodology introduced in this section can be divided into linear and nonlinear schemes. While the former are very fast and often of sufficient accuracy, the nonlinear iterative solvers require more computing power and time to come up with a best estimate. The retrieval methods are tailored to address the issue of albedo-related biases, which arises due to correlations with broad-band absorption features resulting from the instrument's low spectral resolution.

**Left column (original):**

estimate. The retrieval methods are taylored to remedy the problem of albedo related biases due to correlation with broad band absorption features caused by the instrument's low spectral resolution.

## 2.1 Experimental Setup

The measured spectra analyzed in the study at hand were acquired during the COMET (Carbon diOxide and METhane) campaign with the DLR HySpex sensor system. This airborne imaging spectrometer, which consists of two commercially available hyperspectral cameras (a VNIR-1600 and a SWIR-320m-e) is described in detail in (IMF) and references therein.
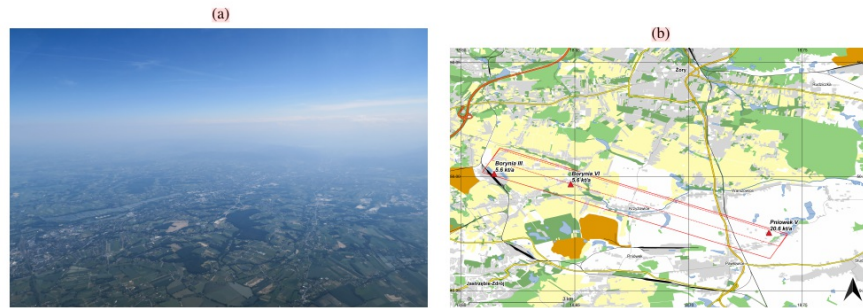
**Figure 1. (a)** View from the aircraft into the mountains around Zywiec at 10 UTC on June 07, 2018. **(b)** In the depicted flight track ("scene 09") the aircraft was on a 115 degrees eastbound heading at ≈ 1.5 km above mean sea level. The map was created with QGIS using OpenStreetMap data (OpenStreetMap contributors, 2022).

The data analyzed in the following chapters was collected during a survey flight conducted within the scope of the CoMet campaign on June 7th, 2018. The CoMet campaign focused on the detection and characterization of $CO_2$ and $CH_4$ sources in the Upper Silesian Coal Basin in southern Poland. It featured a number of ground-based and airborne measurements with both in-situ and remote sensing instruments. The HySpex survey was intended as a feasibility study to evaluate whether – and if so how accurate – localized methane emissions can be retrieved from the SWIR-320m-e data. To achieve this goal we planned 18 flight lines at two different altitudes over a number of known ventilation shafts around Katowice. The location and estimated emission rate of the ventilation shafts was taken from the CoMet ED v1 inventory assembled by Nickl et al. (2020). It was not known in advance, though, which of these ventilation shafts would be actively emitting methane during the day of the survey, as the emission rates are derived from monthly averages reported by the mining companies operating the shafts. The weather during the survey was well suited for remote sensing measurements. Apart from very few occasional patches of thin cirrus clouds there were no further low or mid-level clouds. However, a significant amount of haze could be observed from the aircraft. This can be seen in Image 1a, which displays a view from the aircraft towards the mountains around Bielsko-Biala,

**Right column (revised):**

The data analyzed in this study was collected with the DLR HySpex sensor system during a survey flight conducted within the scope of the COMET (Carbon diOxide and METhane) campaign on June 7th, 2018. The CoMet campaign focused on the detection and characterization of $CO_2$ and $CH_4$ sources in the Upper Silesian Coal Basin (USCB) in southern Poland.
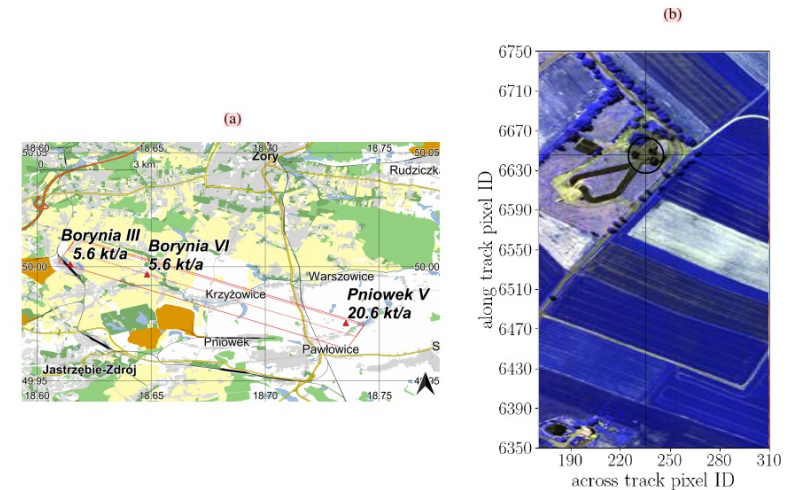
**Figure 1. (a)** Flight lines 09 and 11 are illustrated as a dashed red line and a solid red line, respectively. Flight line 9 was obtained around 09:55 UTC, while Flight line 11 was acquired around 10:10 UTC. The aircraft flew at an altitude of approximately ≈ 1.200 m and ≈ 2.600 m above ground level, respectively, while heading eastward at 115 degrees. The map was generated using QGIS software and OpenStreetMap data (OpenStreetMap contributors, 2022). **(b)** False color image from the SWIR-320m-e camera around the three Pniovek V shafts in scene 09.

The airborne imaging spectrometer HySpex consists of two commercially available hyperspectral cameras (a VNIR-1600 and a SWIR-320m-e) and its basic specifications are presented in Table 1. The aim of this survey was to conduct evaluate the feasibility of localized methane emission retrieval using the SWIR-320m-e data. To achieve this goal we planned 18 flight lines at two different altitudes over a number of known ventilation shafts around Katowice. However, it was not known in advance which of these ventilation shafts would be actively emitting methane during overpass, because only monthly averages of the emission rates are reported by the mining companies operating the shafts Nickl et al. (2020).

located approximately 20 km southeast of the survey area. Actual wind data for the USCB area on the measurement day is

110 presented in Luther et al. (2022, Fig. 4 and 6).

Since this study compares the performance of various retrieval methods, we restrict our analysis to the two flight lines: Flight line 9, acquired at 1200 m above ground level (AGL) around 0955 UTC and flight line 11 acquired at 2600 m AGL around 1010 UTC. The respective foot prints of line 9 (dashed red line) and line 11 (solid red line) are shown in Fig. 1b along with the location and estimated emission rate of the three ventilation shafts (red triangles) located within. Each track took the aircaft

115 $\approx$ 3 minutes during which 7130 (scene 09) and 5075 (scene 11) along track observations for each of the 320 across track detector pixels were acquired.

In Fig. 2b an ensemble of along track averaged HySpex measurements are depicted. The sensor's sampling distance across the spectral axis is indicated by the vertical grid lines which is not constant in the wavenumber domain. The spectral coverage of the HySpex SWIR-320m-e camera ranges from 967–2496 nm (4005–10338 cm$^{-1}$), with the exact number depending on the

120 across track pixel ($\approx \pm 1$ cm$^{-1}$). The spectral resolution, i. e., the full width at half maximum (FWHM) of the HySpex SWIR-320m-e camera in the 4000–6500 cm$^{-1}$ region ranges from 6.0–9.5 nm (10–40 cm$^{-1}$). Its values are provided for each across track pixel of the detector (a 2D array) with the level 1b data set. This data set was basically created as described in Lenhard et al. (2015), except for the optical distortion correction. The Instrument Spectral Response Function (ISRF) calibration was performed according to Baumgartner (2021). Hence, the ISRF for each pixel is available as a lookup table with an sampling

125 distance of 1.2 nm. The standard HySpex product is corrected for optical distortions and resampled to a constant spectral resolution and across-track resolution using the method described in Baumgartner and Köhler (2020). For this study, this processing step was ommited.

**Table 1.** Summary of some important HySpex properties. The sensor is described in detail in (IMF) and references therein.

| HySpex specifications | |
|---|---|
| Detector | MCT Sofradir MARS |
| Spectral Range [nm] | 968-2498 |
| Field of View (with FoV Expander) [°] | 13.2 / 27.2 |
| Number of (spectral) Channels | 256 |
| Sampling Interval [nm] | 6.0 |
| Bandwidth [nm] | 5.6–7.0 |
| Number of (geometric) Pixels | 320 |
| Dynamic Range [bit] | 14 |

The weather during the survey was well-suited for remote sensing measurements. Apart from very few occasional patches of thin cirrus clouds there were no further low or mid-infrared-level clouds. However, some amount of haze was observed from the aircraft during the flights. Actual wind data for the USCB area on the measurement day is presented in Luther et al. (2022, Fig. 4 and 6). Fig. 1 displays the flight tracks over the Pniovek V and other two shafts. It took the aircraft approximately three

105 minutes to complete one track, during which time 7130 (scene 09) and 5075 (scene 11) observations were recorded for each of the 320 across-track detector pixels. To compare the effectiveness of various retrieval methods, we limit our analysis to the two flight lines shown in Fig. 1a, namely Flight line 9 (called scene 09) and Flight line 11 (called scene 11). The map also depicts the location of the potential sources with their nominal (reported) emission rates.
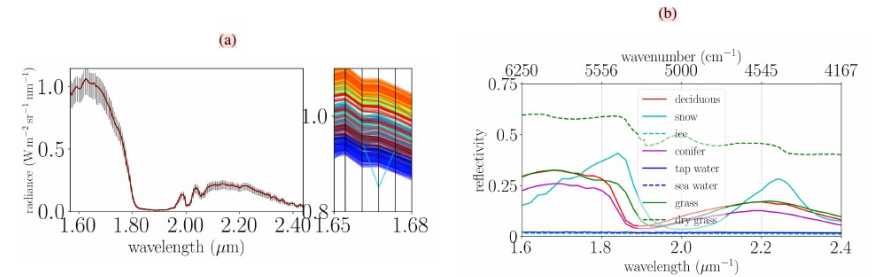
**Figure 2. (a)** HySpex average spectrum with the span (minimum to maximum) depicted in gray for measurements across the 320 across track detector pixels for scene 09 (left). The center shows a bunch of individual spectra around 1.67 $\mu$m with the black lines indicating the pixel positions and sampling distance. The radiance values of pixel 104 (cyan) at $\approx$ 1.677 $\mu$m (5960 cm$^{-1}$), which is relevant for the CH4 retrieval appears to be problematic. **(b)** Reference reflectances for different surface types (measured at the John Hopkins University).
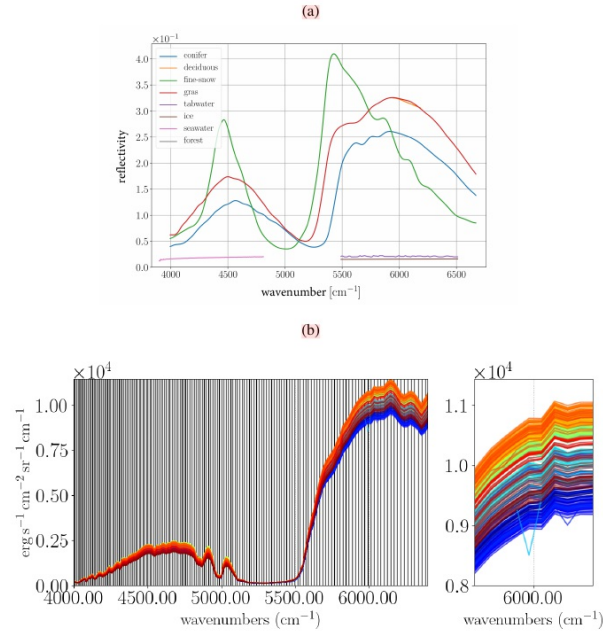
**Figure 2. (a)** Reference reflectances for different surface types (measured at the John Hopkins University). **(b)** HySpex measurements across the 320 detector pixels (from blue to red, left to right). The radiance values of across track pixel 104 (cyan) for wavenumber $5960\,\mathrm{cm}^{-1}$ (relevant for the CH4 retrieval) appear to be problematic.

As pointed out, it is the rather low spectral resolution that makes the retrieval of atmospheric constituents challenging. Figure 2 shows reflectances for various surface types along track averaged Hyspex spectra. Note that the radiative intensity in the interval around $6000\,\mathrm{cm}^{-1}$ is significantly larger compared to the radiance between $4000$–$5000\,\mathrm{cm}^{-1}$. The measurement is only able to resolve broad band molecular absorption features since the high frequency variations are smoothed by the coarse instrument resolution (see absorption from methane's $2\nu_3$ band around $6000\,\mathrm{cm}^{-1}$). The figure also indicates a possible bad pixel with systematically lower radiance values along the flight track, just below $6000\,\mathrm{cm}^{-1}$, corresponding to across track pixel 104 (a descending cyan line).

In Fig. 2a an ensemble of along track averaged HySpex measurements is depicted. The sensor's sampling distance across the spectral axis is indicated by the vertical grid lines. The spectral coverage of the HySpex SWIR-320m-e camera ranges from $967$–$2496\,\mathrm{nm}$ ($4005$–$10338\,\mathrm{cm}^{-1}$), with the exact number depending on the across track pixel ($\approx \pm 1\,\mathrm{cm}^{-1}$). The figure shows that the radiative intensity in the interval around $1.6\,\mu\mathrm{m}$ ($\approx 6000\,\mathrm{cm}^{-1}$) is significantly larger than that between $2.3\,\mu\mathrm{m}$ ($\approx 4300\,\mathrm{cm}^{-1}$) mostly due to $H_2O$ absorption.

The values for the spectral resolution, i.e., the full width at half maximum (FWHM) of the SWIR-320m-e camera in the $1500$–$2500\,\mathrm{nm}$ ($4000$–$6500\,\mathrm{cm}^{-1}$) region ranges from $6.0$–$9.5\,\mathrm{nm}$ ($10$–$40\,\mathrm{cm}^{-1}$), are provided for each across track pixel of the detector (a 2D array) with the level 1b data set. This data set was basically created as described in Lenhard et al. (2015), except for the optical distortion correction. The Instrument Spectral Response Function (ISRF) calibration was performed according to Baumgartner (2021). Hence, the ISRF for each pixel is available as a lookup table with an sampling distance of $1.2\,\mathrm{nm}$.

Figure 2b displays reference reflectances for various surface types across the same spectral interval. Due to the instrument's coarse spectral resolution, the measurement is only capable of resolving broad-band molecular absorption features. A possible bad pixel is shown in the figure around $1.65\,\mathrm{nm}$ (a descending cyan line) which shows with systematically lower radiance values along the flight track. The pixel corresponding to across track pixel 104.

## 2.1 Radiative transfer

In the SWIR spectral range the radiative transfer through the atmosphere under clear sky conditions (cloud and scattering free in general) is well described by Beer's law (Zdunkowski et al., 2007) with the monochromatic transmission in wavenumbers $\nu$ given by

$$\mathcal{T}_m(\nu; s) = \exp\left(-\sum_m \tau_m(\nu, s)\right) = \exp\left(-\int_{\text{path}} ds \sum_m n_m(s)\,k_m\big(\nu, p(s), T(s)\big)\right). \tag{1}$$

The model assumes a pure gas atmosphere with molecular $m$ optical depth $\tau$ given by the path integral along $s$ over the molecular number densities $n_m$ and $k_m$, the pressure $p$ and temperature $T$ dependent absorption cross section. This study utilizes the 2020 spectroscopic line data from GEISA (Gestion et Etude des Informations Spectroscopiques Atmosph'eriques; Delahaye et al., 2021) for molecular absorption calculations.

## 2.2 Radiative transfer

In the SWIR spectral range the radiative transfer for a down and up path through the atmosphere under clear sky conditions (cloud free) is well described by Beer's law (Zdunkowski et al., 2007) with the monochromatic transmission from Top of Atmosphere (TOA) to Bottom of Atmosphere (BOA) given by

$$\mathcal{T}_m(\nu; s) = \exp\left(-\sum_m \tau_m(\nu, s)\,\mathrm{d}s\right) = \exp\left(-\int_{\text{path}} \mathrm{d}s \sum_m n_m(s)\,k_m\big(\nu, p(s), T(s)\big)\right). \tag{1}$$

The model assumes a pure gas atmosphere with molecular optical depth $\tau$ given by the path integral over the molecular number densities $n_m$ and $k_m$, the pressure and temperature dependent absorption cross section.

In conditions where particles such as haze, dust or high clouds prevail, extinction (scattering and absorption) by aerosols should be taken into account (De Leeuw et al., 2011). Aerosol optical thickness $\tau_{\text{aer}}$ at wavenumber $\nu$ is often described by a power law

$$\tau_{\text{aer}}(\nu) = \tau_{\text{aer}}(\nu_0)\left(\frac{\nu}{\nu_0}\right)^{\beta}, \tag{2}$$

where $\tau_{\text{aer}}(\nu_0)$ is the optical thickness at a reference wavenumber and $\beta$ a parameter for the aerosol. The Ångstrom exponent $\beta$ typically ranges from $1 \leq \beta \leq 2$ (Liou, 2002) and while it is close to 1.0 for almost clear sky conditions with weak scattering by haze or dust, it is assumed to increase for hazy conditions. In analogy to $k_m$ the aerosol cross section can be defined as

$$\tau_{\text{aer}}(\nu_0) = \int_{\text{path}} k_{\text{aer}}(\lambda_0)\,n_{\text{air}}(s)\,\mathrm{d}s = N_{\text{air}}\,k_{\text{aer}}(\lambda_0)\left(10^4/\nu\right)^{-\beta} \tag{3}$$

with $\lambda_0 = 1\,\mu\text{m}$ and $k_{\text{aer}}(\nu)$ proportional to $\lambda^{-\beta}$ according to

$$k_{\text{aer}}(\lambda) = k_{\text{aer}}(\lambda_0)/\lambda^{\beta} \quad \text{and} \quad k_{\text{aer}}(\lambda_0) = 1.4 \cdot 10^{-27}. \tag{4}$$

## 2.3 Model atmosphere setup

The model atmosphere's vertical extent ranges from 0–80 km with 39 levels in total. The atmosphere is composed by pure gaseous layers above $z_{\text{mol}} = 10\,\text{km}$ and layers containing gases and particles below $z_{\text{sc}} = 10\,\text{km}$. The vertical resolution is highest in the (plume) layer below $z_{\text{pl}} = 2\,\text{km}$ where the enhancement is expected to takes place (see Fig. 3). The $CH_4$ optical depth is modeled in terms of a climatological background and a Gaussian plume

$$\tau_{CH_4} = \tau_{\text{bg}} + \alpha_{CH_4}\,\tau_{\text{pl}}. \tag{5}$$

Although the shape of the plume profile is not crucial as the nadir viewing geometry does not allow to retrieve information on the vertical distribution of trace gases in the SWIR (see Buchwitz et al. (2000, Sec. 3)) our setup constrains the fit to the lowest atmospheric layer up to 2.0 km (see Thorpe et al. (2014, 5.2)).
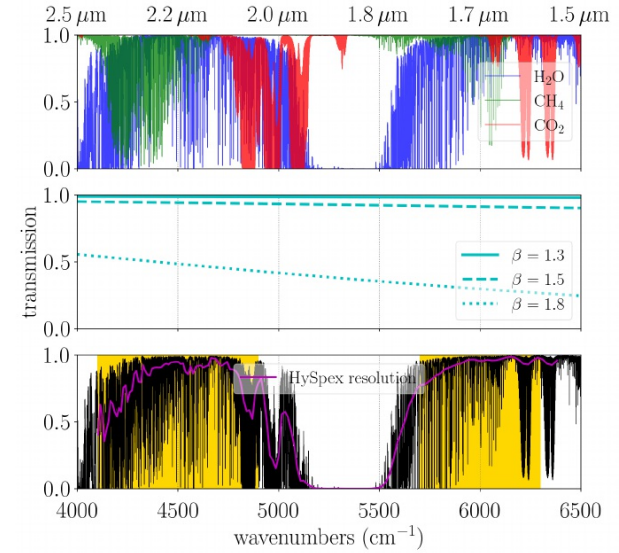
**Figure 3.** Monochromatic transmissions of $CH_4$, $CO_2$ and $H_2O$ for the SWIR spectral range and a nadir looking observer at 1.5 km at a solar zenith angle (SZA) of 30° are depicted in the top panel. The aerosol transmission in the mid-infrareddle panel has only smooth variations across the spectrum. The magenta line in the lower panel represents the total transmission degraded to HySpex resolution. The spectral intervals used for the $CH_4$ fit are indicated by the yellow background. The two fitting windows range from 4100–4900 $\text{cm}^{-1}$ (4K) and 5700–6300 $\text{cm}^{-1}$ (6K), respectively. Note significant differences in transmissions of the monochromatic spectrum and convolved instrument spectrum.

In conditions where particles such as haze, dust or high clouds prevail, extinction (scattering and absorption) by aerosols should be taken into account (De Leeuw et al., 2011). Aerosol optical thickness is often described by a simple power law with an exponent $\beta$ (details see Hochstaffl (2022)). The mid-infrareddle panel in Fig. 3 exemplary depicts such a model's result for different exponents.

In Fig. 3, the top panel shows the individual components of the monochromatic total transmission for the US-Standard atmosphere, including methane's first overtone of the fundamental vibrational transition $2\nu_3$ (with its P and R branches) around 6000 $\text{cm}^{-1}$ (1560-1660nm, tetradecad band), as well as additional strong absorption lines ranging from 4200–4600 $\text{cm}^{-1}$ (2090-2290nm, octad). The bottom panel illustrates how the observer's coarse spectral resolution smooths the total monochro-

The $CH_4$ background as well as the $CO_2$ initial guesses are modeled according to the Air Force Geophysical Laboratory (AFGL, Anderson et al., 1986) atmospheric constituent profiles scaled to 1875 ppb and 400 ppm, respectively. The molecules $H_2O$ as well as the auxiliary parameters temperature and pressure are taken from reanalysis data provided by the National Center for Environmental Prediction (NCEP, Kalnay et al., 1996).
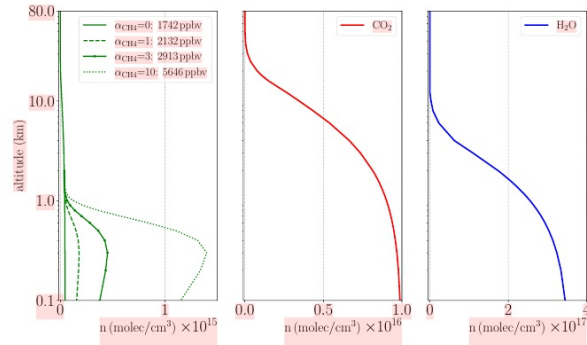
**Figure 3.** Atmospheric vertical profiles of molecular number densities $n_m$ for $CH_4$, $CO_2$, and $H_2O$. The $CH_4$ profile is split into two components, i. e., a reference (background) profile ranging from BoA to ToA and a Gaussian plume enhancement $< 2$ km which is scaled by $\alpha_{CH4}$. Beside $CH_4$ the well mixed $CO_2$ profile is depicted in the middle while an initial guess for $H_2O$ is shown on the right.

**2.4 Beer InfraRed Retrieval Algorithm (BIRRA)**

The BIRRA level 2 processor was originally developed at the Deutsches Zentrum für Luft- und Raumfahrt (DLR) and comprises the line-by-line forward model Generic Atmospheric Radiation Line-by-line InfraRed Code (GARLIC, Schreier et al., 2014) coupled to a least squares solver for trace gas retrieval in the SWIR spectral region (Hochstaffl et al., 2018). It has been successfully applied to SCIAMACHY (Scanning Imaging Absorption Spectrometer for Atmospheric Chartography, Gimeno García et al., 2011; Hochstaffl and Schreier, 2020) and TROPOMI (TROPOspheric Monitoring Instrument, Hochstaffl et al., 2020) observations. The BIRRA retrievals in this study are based on a Python reimplementation of the validated (Fortran) code (Gimeno García et al., 2011; Hochstaffl et al., 2018). The radiative transfer computations are hence based on Py4CAtS (Python for Computational Atmospheric Spectroscopy, (Schreier et al., 2019)), a Python reimplementation of GARLIC.

The mathematical forward model $\Phi(\boldsymbol{x},\nu)$ describes the measured intensity spectrum $I(\nu)$ for a nadir looking observer according to

$$\Phi(\boldsymbol{x},\nu) = \frac{r(\nu)}{\pi}\cos(\theta)\,I_{\mathrm{sun}}(\nu)\,\mathcal{T}_m^{\downarrow}(\nu)\,\mathcal{T}_m^{\uparrow}(\nu) \otimes S(\gamma(\nu))\,, \qquad (6)$$

---

matic transmission (shown in black). There are 67 and 28 HySpex pixels used by the retrievals within the range of the 4K and 6k spectral windows, respectively.

**2.2 Model atmosphere setup**

The model atmosphere's vertical extent ranges from 0–80 km with 39 levels in total. The atmosphere is composed of pure gaseous layers above altitude $z = 10$ km and layers containing gases and particles below $z = 10$ km. The vertical resolution is highest in the (plume) layer below $z_{\mathrm{pl}} = 2$ km where the enhancement is expected to takes place. The $CH_4$ optical depth is modeled in terms of a climatological background and a Gaussian plume

$$\tau_{CH_4} = \tau_{\mathrm{bg}} + \alpha\,\tau\,, \qquad (2)$$

where $\alpha$ represents the molecular scaling factor for the plume optical depth while $\tau_{\mathrm{bg}}$ represents the background.

Although the shape of the plume profile is not crucial as the nadir viewing geometry does not allow to retrieve information on the vertical distribution of trace gases in the SWIR (see Buchwitz et al., 2000, Sec. 3) our setup constrains the fit to the lowest atmospheric layer up to 2.0 km (see Thorpe et al., 2014, 5.2).

The $CH_4$ background profile as well as the $CO_2$ background profile are modeled according to the Air Force Geophysical Laboratory (Anderson et al., 1986, AFGL) atmospheric constituent profiles scaled to 1875 ppb and 400 ppm, respectively. The molecules $H_2O$ as well as the auxiliary parameters temperature and pressure are taken from reanalysis data provided by the National Center for Environmental Prediction (Kalnay et al., 1996, NCEP).

**2.3 Beer InfraRed Retrieval Algorithm (BIRRA)**

The *BIRRA level 2 processor*, developed at DLR, uses the line-by-line forward model Generic Atmospheric Radiation Line-by-line InfraRed Code (Schreier et al., 2014, GARLIC) and a separate (SLS) or nonlinear least squares solver (NLS) for trace gas retrieval in the SWIR spectral region (Hochstaffl et al., 2018). It has been successfully applied to SCIAMACHY (Scanning Imaging Absorption Spectrometer for Atmospheric Chartography, Gimeno García et al., 2011; Hochstaffl and Schreier, 2020) and TROPOMI (TROPOspheric Monitoring Instrument, Hochstaffl et al., 2020) observations. In this study, however, the new Python version of BIRRA is used which is based on Py4CAtS (Python for Computational Atmospheric Spectroscopy, (Schreier et al., 2019)), a Python reimplementation of the validated Fortran code GARLIC (Schreier et al., 2013).

The mathematical forward model $\Phi(\boldsymbol{x},\nu)$ describes the measured intensity spectrum $I(\nu)$ for a nadir looking observer according to

$$\Phi(\boldsymbol{x},\nu) = \frac{r(\nu)}{\pi}\cos(\theta)\,I_{\mathrm{sun}}(\nu)\,\mathcal{T}_m^{\downarrow}(\nu)\,\mathcal{T}_m^{\uparrow}(\nu) \otimes S(\gamma(\nu))\,, \qquad (3)$$

where $r$ refers to the surface reflectivity and $\theta$ represents the solar zenith angle. The terms $\mathcal{T}_m^{\downarrow}$ and $\mathcal{T}_m^{\uparrow}$ denote the total transmission between Sun and reflection point (e.g. the Earth) and between reflection point and observer, respectively (see Eq. 1). The transmission by aerosols for different Ångstrom exponents according to is depicted in Fig. 3 (center). Its behavior can be

where $r$ refers to the surface reflectivity and $\theta$ represents the solar zenith angle. The terms $\mathcal{T}_m^{\downarrow}$ and $\mathcal{T}_m^{\uparrow}$ denote the total transmission between Sun and reflection point (e.g. the Earth) and between reflection point and observer (e.g. the HySpex sensor), respectively. The transmission by aerosols for different Ångstrom exponents according to Eq. (2) is depicted in Fig. 4 (center).

180 Its behavior can be represented by a low order polynomial hence the forward's model total transmission is described as

$$\mathcal{T}_m(\nu;s) = \exp\left(-\sum_m \alpha_m \tau_m(\nu) - \sum_{i>0} a_i \nu^i\right). \tag{7}$$

The unknown (to be estimated) parameters are composed as elements of the state vector $x$ and include the molecular scaling factors $\alpha_m$, the aerosol coefficients $a_i$, and the coefficients for the surface reflectivity $r_j$ (with $j \geq 0$) which is also modeled by a polynomial. Note that since the information of the vertical profile is well under-determined in the observed spectrum scaling

185 factors $\alpha_m$ for the initial guess profiles are retrieved (Gimeno García et al., 2011, Fig. 1). Finally, the instrument's spectral response is described by the spectral response function (SRF) $S$. Its parameters such as the half width $\gamma$ or a spectral shift can (optionally) be part of the state vector.

---

represented by a low order polynomial hence the forward's model total transmission is described as

$$\mathcal{T}_m(\nu;s) = \exp\left(-\sum_m \alpha_m \tau_m(\nu) - \sum_{i>0} a_i \nu^i\right). \tag{4}$$

The unknown (to be estimated) parameters are composed as elements of the state vector $x$ and include the molecular scaling factors $\alpha_m$, the aerosol coefficients $a_i$, and the coefficients for the surface reflectivity $r_j$ (with $j \geq 0$) which is also modeled by

175 a polynomial. Note that since the information of the vertical profile is well under-determined in the observed spectrum scaling factors $\alpha_m$ for the initial guess profiles are retrieved (Gimeno García et al., 2011, Fig. 1). Finally, the instrument's spectral response is described by the ISRF $S$. Its parameters such as the half width $\gamma$ or a spectral shift can (optionally) be part of the state vector.

### 2.3.1 Nonlinear solvers

180 This study examines various nonlinear retrieval schemes that were implemented in the BIRRA level 2 processor and are briefly introduced below. Nonlinear least squares methods are iterative and require calculating derivatives for each of the nonlinear state vector elements across the spectral axis, represented by a Jacobian matrix J. Note that $||\cdot||$ represents the 2-norm throughout this study.

**Nonlinear (NLS) and separable least squares (SLS)**

185 The nonlinear least squares fit minimizes the objective function $\mathcal{L}$ for given measurements $y$ according to

$$\min_x ||y - \Phi(x)||^2, \tag{5}$$

and applies when the model function $\Phi$ is nonlinear in one or more parameters of $x$.

The so called separable least squares solver splits (separates) the state vector $x$ into nonlinear and linear parameters $x = (\eta, \zeta)$ where the elements in $\zeta$ enter the forward model $\Phi$ linearly (see Sec. 2.4.1). The minimization problem is hence given

190 by

$$\min_{\eta, \zeta} ||y - \Phi(\eta)\zeta(\eta)||^2. \tag{6}$$

This setup is also known as the Variable Projection (VarPro, Golub and Pereyra, 2003) method where $\eta$ is independent of $\zeta$ in the matrix product $\Phi(\eta)\zeta(\eta)$. The parameters in $\eta$ can hence be fitted in the usual way by means of Gauss–Newton or Levenberg–Marquardt algorithms (Hansen et al., 2013, see).

195 **Generalized least squares (GLS)**

To account for correlated errors, a generalized least squares fit is used. The covariance matrix C takes into account the spectral variations of the scene's background, which includes parts of the flight track that are not affected by the $CH_4$ plume. To create the matrix C, the location of the point source and wind data must be known. The spectral covariance for a given
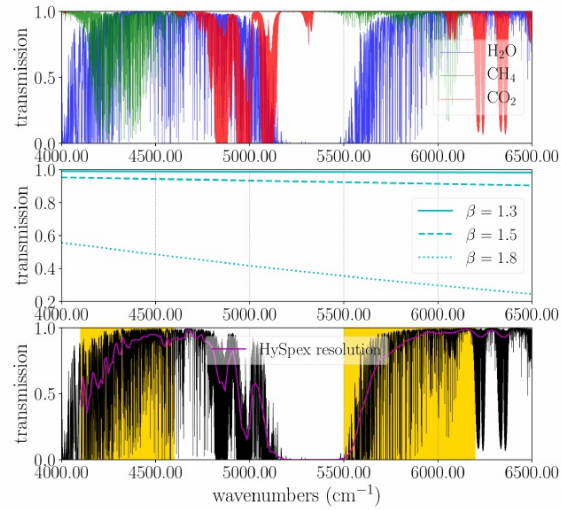
**Figure 4.** Monochromatic transmissions of $CH_4$, $CO_2$ and $H_2O$ for the SWIR spectral range and a nadir looking observer at 1.5 km at a solar zenith angle (SZA) of $30°$ are depicted in the top panel. The aerosol transmission in the middle panel shows only smooth variations across the spectrum. The magenta line in the lower panel represents the total transmission degraded to HySpex resolution and the spectral intervals with methane absorption are indicated by the yellow background. Also note significant differences in transmissions of the monochromatic spectrum and convolved instrument spectrum.

The molecular absorption calculations in this study exploit GEISA (Gestion et Etude des Informations Spectroscopiques Atmosphériques; Delahaye et al., 2021) 2020 spectroscopic line data. In the top panel of Fig. 4 the individual components of the monochromatic total transmission for the US-Standard atmosphere are shown. Methane's first overtone of the fundamental vibrational transition $2\nu_3$ (with its P and R branches) is found around $6000\,\mathrm{cm}^{-1}$ while additional (strong) absorption lines range from $4100$–$4700\,\mathrm{cm}^{-1}$ (band center $\approx 4420\,\mathrm{cm}^{-1}$). The panel at the bottom demonstrates how the total monochromatic transmission (in black) is smoothed by the observer's coarse spectral resolution.

In Fig. 5 the BIRRA Jacobian matrix for two spectral intervals with strong methane absorption is depicted, respectively.

scene is computed to account for possible background variations similar to methane band absorption that could be mistakenly interpreted as a molecular enhancement. Fig. 4 shows the covariance matrices for the methane retrieval intervals.

The error covariance matrix $\mathsf{C}$ is a symmetric positive semi-definite matrix that is precomputed for each flight track. To account for correlated errors, the non-negative square root matrix $\mathsf{S} = \mathsf{C}^{1/2}$ is used to estimate $\boldsymbol{x}$ by minimizing the 2-norm of the weighted residual vector:

$$\min_{\boldsymbol{x}} ||\mathsf{S}^{-1}(\boldsymbol{y} - \boldsymbol{\Phi}(\boldsymbol{x}))||^2. \tag{7}$$
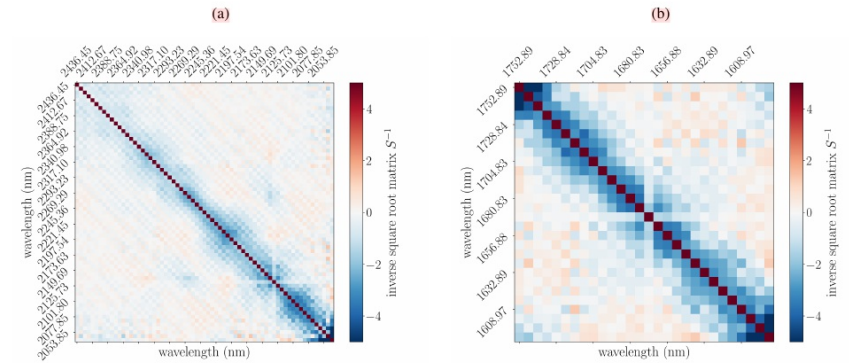
**Figure 4.** Scene 09 background covariance matrix for the **(a)** 4100-4900 $\mathrm{cm}^{-1}$ (4K, left) and **(b)** 5700-6300 $\mathrm{cm}^{-1}$ (6K, right) spectral range. The background area was defined outside of the pixels along-track=$(6300, 6670)$, across-track=$(180, 285)$. Note that beside the bad HySpex pixel mentioned in Fig. 2 at $5992.74\,\mathrm{cm}^{-1}$ there appears to be another suspect pixel at $4691.04\,\mathrm{cm}^{-1}$.

### 2.3.2 Methane enhancement estimate for nonlinear solvers

The state vector $\boldsymbol{x}$ for the methane plume fit comprises the $CH_4$ scaling factor and a second-order reflectivity polynomial per spectral window. Further parameters were found to be unnecessary as they did not improve the retrieval outcome but rather destabilized the solutions, owing to an increase in the condition number of the Jacobi matrix.

A scene averaged spectrum, excluding ground pixels around the suspected $CH_4$ sources, was employed to estimate $H_2O$, $CO_2$ and $CH_4$ background concentrations. The $CO_2$ background level of the scene is inferred from the $1.6\,\mu$m and $2\,\mu$m bands via a multi-interval (4K and 6K spectral windows) fit. A scene averaged background scaling factor of $\tilde{\alpha}_{CO2} = 0.96$ for scene 09 and $\tilde{\alpha}_{CO2} = 0.93$ for scene 11 was found. Due to the degeneracy between $H_2O$ and the reflectivity polynomial at HySpex's spectral resolution the scene averaged $H_2O$ scaling factor should be viewed as effective parameter that partly captures low frequency components in the spectrum. The scene averaged $CH_4$ background profile was found to be within 5 % of the initial guess of 1875 ppbv, hence it was maintained and not scaled.
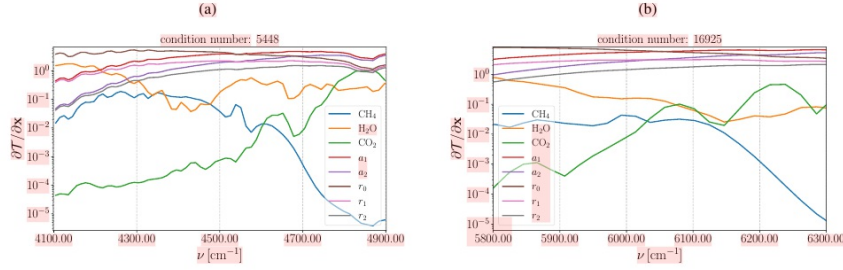
**Figure 5.** Columns of the Jacobian matrix and condition numbers in the $4100$–$4900\,\mathrm{cm}^{-1}$ (left) and $5800$–$6300\,\mathrm{cm}^{-1}$ (right) spectral intervals.

### 2.4.1 Nonlinear least squares solvers

Various nonlinear retrieval schemes were examined and are briefly introduced subsequently. The iterative nature of nonlinear least squares methods requires the calculation of derivatives for each of the nonlinear state vector elements across the spectral axis which is represented by the Jacobian matrix J. The feasibility of a given retrieval setup is briefly studied after the introduction of the various solvers in Sec. 3.1.1. Therefore the condition number of the Jacobians are examined for different spectral intervals relevant for the SWIR $CH_4$ retrieval.

The retrieval's performance, e.g., the fit quality, is assessed with respect to the 2-norm of the discrepancy between the measurement $\boldsymbol{y}$ and the converged spectrum $\sigma = \|\boldsymbol{y} - \boldsymbol{I}(\boldsymbol{x})\|_2$, also known as the residual norm. The least squares (error) covariance matrix is given by

$$\Xi \;=\; \frac{\sigma^2}{(m-n)}\,(\mathrm{J}^\mathrm{T}\mathrm{J})^{-1} \tag{8}$$

where J represents the Jacobi matrix, while $m$ and $n$ specify the number of measurements and number of state vector elements, respectively. The errors of the individual state vector parameters are obtained from the diagonal elements of $\Xi$.

**Nonlinear least squares (NLS)**

The nonlinear least squares fit minimizes the objective function $\mathcal{L}$ for given measurements $\boldsymbol{y}$ according to

$$\min_{\boldsymbol{x}}\left\{\mathcal{L}(\boldsymbol{x})\right\} \;=\; \min_{\boldsymbol{x}}\|\boldsymbol{y} - \boldsymbol{\Phi}(\boldsymbol{x})\|_2^2\,, \tag{9}$$

and applies when the model function $\boldsymbol{\Phi}$ is nonlinear in one or more parameters of $\boldsymbol{x}$.

The decision to exclude aerosol parameters from the $CH_4$ plume fit was encouraged by findings from Borchardt et al. (2021), who concluded that different aerosol scenarios in the SWIR do not induce errors greater than 0.2 %. Moreover, since the spectra were observed at low flight altitudes on a rather clear day (see Fig. 1 and Luther et al. 2019), retrieval errors induced by aerosol scattering should be negligible in our scenario as well (also see Fig. 3 and Thorpe et al. 2013; Thompson et al. 2015). Nonetheless the study accounts for light path modifications in the reported $CH_4$ estimates by using the scene average $\alpha_{CO2}$ scaling factor from above. The actual $CH_4$ column given by the background concentration plus the retrieved enhancement includes corrections for light path modifications via the prefitted scene averaged background $CO_2$ $\tilde{\alpha}_{CO2}$ given by

$$N_{CH4} \;=\; N_{bg} + \frac{\alpha}{\tilde{\alpha}_{CO2}}\,\hat{N}_{pl}(z_0)\,, \tag{8}$$

with

$$\hat{N}_{pl}(z_0) \;=\; \int_{z_0}^{z_{pl}} n_{pl}(z)\,\mathrm{d}z\,, \tag{9}$$

and $z_0$ representing the bottom of the atmosphere. Note that this approach assumes that the $CO_2$ profile upon which $\tilde{\alpha}_{CO2}$ was estimated corresponds to the true profile and that $\tilde{\alpha}_{CO2}$ is 1 in absence of scattering. The actual retrieval fits the methane enhancement factor along with a second order reflectivity polynomial so that the state vector is given by $\boldsymbol{x} = (\alpha, r_0, r_1, r_2)$. This setup is found robust toward lower SNR values and less prone to correlations across state variables.

### 2.4 Linear solvers

In contrast to nonlinear fitting schemes, linear solvers for $\boldsymbol{x}$ can only be used when equations can be expressed as a linear combination of the variables in $\boldsymbol{x}$. To utilize such methods, it is usually required to linearize the forward model with respect to the variables of interest. The solvers can be split into two groups, i. e., one that take background statistics into account (MF and SVD) and the two others that do not (LLS and SSD).

### 2.4.1 Linear least squares (LLS)

The LLS method uses a linear fitting scheme to estimate the $CH_4$ parameter (see Eq. 2). Assuming that the increase in optical depth caused by the plume, $\tau$, is relatively small, the BIRRA forward model from Sec. 2.3 is linearized with respect to $\alpha$ by approximating the transmission spectrum of the plume by Taylor expansion according to

$$\exp(-\tau) \;\approx\; (1 - \alpha\,\tau)\,. \tag{10}$$

The linear least squares problem of $M$ measurements can then be formulated according to

$$\min_{\boldsymbol{x}}\|\boldsymbol{y} - \boldsymbol{\Phi}\,\boldsymbol{x}\| \tag{11}$$

where the model functions in $\boldsymbol{\Phi}$ for the linear parameters of the state vector $\boldsymbol{x} = (r_0, b_0 = r_0\,\alpha)$ are given by

$$\phi_1 \;=\; \frac{\cos(\theta)}{\pi}\,I_{sun}\,\mathcal{T}^{\downarrow}\mathcal{T}^{\uparrow} \otimes S\,, \tag{12}$$

$$\phi_2 \;=\; -\frac{\cos(\theta)}{\pi}\,I_{sun}\,\mathcal{T}^{\downarrow}\mathcal{T}^{\uparrow}\tau \otimes S\,. \tag{13}$$

**Separable least squares (SLS)**

The so called separable least squares solver splits (separates) the state vector $x$ into nonlinear and linear parameters $x = (\eta, \beta)$ where the elements in $\beta$ enter the forward model $\Phi$ linearly (see Sec. 2.5) while the components in $\eta$ are of nonlinear nature. The minimization problem is hence given by

215
$$\min_{\eta,\beta} \| y - \Phi(\eta)\beta(\eta) \|_2^2 . \tag{10}$$

This setup is also known as the Variable Projection (VarPro, Golub and Pereyra, 2003) method where $\eta$ is independent of $\beta$ in the matrix product $\Phi(\eta)\beta(\eta)$. The parameters in $\eta$ can hence be fitted in the usual way by means of Gauss–Newton or Levenberg–Marquardt algorithms (see e. g. Hansen et al. (2013)).

**Generalized least squares (GLS)**

220 A so called generalized least squares fit can be employed to account for correlated errors. The covariance matrix $C$ is used to account for the spectral variations of the scene's background, i. e.parts of the flight track which are presumably not influenced by the $CH_4$ plume. Therefore, the location of the point source along with wind data needs to be knows. The matrix $C$ is then created by computing the spectral covariance for a given scene. The idea is that possible background variations similar to the methane band absorption are not (mistakenly) interpreted as a molecular enhancement. The covariance matrices for the 225 methane retrieval intervals are depicted in Fig. 6.

The symmetric positive semidefinite error covariance matrix $C$ is (pre-)computed for a given flight track so that the non-negative square root matrix $S = C^{\frac{1}{2}}$ can be used to estimate $x$ according to

$$\min_{x} \| S^{-1}(\hat{y} - Jx) \|_2^2 . \tag{11}$$

245 It is important to note that with this setup the reflectivity coefficient $r_0$ is present in both elements of the state vector. In order to avoid this and allow for higher order reflectivity polynomials in the fit, which are required for large spectral intervals, the retrieval is performed in two steps. In a first step only the reflectivity coefficients are fitted while in a second step $\alpha$ is estimated with the prefitted reflectivity coefficients given as input. This setup allows fits for an increased spectral interval. In addition, the setup allows for spectral separation by de-weighting individual pixels in the albedo fit that are impacted by 250 methane. This basically ensures that the reflectivity coefficients can be fitted outside the absorption bands of the target, and then the enhancement factor can subsequently be estimated from the range where absorption occurs. This approach minimizes interference between the two fits, preventing the reflectivity polynomial from capturing absorption of $CH_4$.

Another aspect that should be kept in mind is that that since $1 - \alpha\tau \leq \exp(-\alpha\tau)$ for $\alpha \geq 0$ the linearized model underestimates the $CH_4$ enhancement for a given optical depth $\tau$ compared to the nonlinear setup (forward plus inversion). However, 255 the setup should be sensitive enough to yield elevated methane levels.

#### 2.4.2 Matched Filter (MF)

The MF is a well-established method for estimating molecular concentration enhancements from hyperspectral sensors, with numerous studies supporting its effectiveness (Theiler and Foy, 2006; Villeneuve et al., 1999; Funk et al., 2001; Thorpe et al., 2013; Thompson et al., 2015). The linear enhancement factor estimate is derived by perturbing an average (background) 260 radiance spectrum $\mu$ with a known target spectrum $t$. The approach is analogous to that used by Thompson et al. (2015), where $CH_4$ enhancements are estimated by linearly scaling a target signature that perturbs the mean radiance

$$\alpha_i(y) = \frac{(t(\mu))^T C^{-1}(y_i - \mu)}{\sqrt{(t(\mu))^T C^{-1}(t(\mu))}} . \tag{14}$$

This equation constitutes the linear minimizer that solves the Gaussian log-likelyhood

$$\min_{\alpha_i} \| C^{-1/2} d \|^2 \quad \text{with} \quad d = y_i - (\mu + \alpha_i t(\mu)) \quad \text{and} \quad t(\mu) = -\mu\tau . \tag{15}$$

265 The method assumes that the measured spectrum can be represented as a linear superposition of the $CH_4$ plume's optical depth and the mean unperturbed radiance $\mu$ and tests an observed vector $y_i$ against a base vector while accounting for the background covariance $C$. Note that the mean background spectrum $\mu$ and $C$ were computed per scene and the inverse covariance $C^{-1}$ is approximated by decomposing $C$ into eigenvalues and eigenvectors (Thompson et al., 2015, Eq. 6-8).

In order to get a more accurate target spectrum estimate, a per pixel estimate of the target spectrum was computed which 270 accounts for the pixel's albedo (Foote et al., 2020, II. Methods, C.). This albedo normalized matched filter includes an albedo factor $r_i$ for each measurement spectrum according to

$$d_r = y_i - (\mu + r_i\alpha_i t(\mu)) \quad \text{with} \quad r_i = \frac{y_i^T \mu}{\mu^T \mu} \tag{16}$$

According to Guanter et al. (2021), the classical matched filter is relatively sensitive to surface albedo which could be mitigated by k-means clustering of the scene. This approach reduces within-class variance, which in turn should minimize 275 the albedo sensitivity of $\alpha$. In the so called cluster-tuned matched filter, instead of computing a single background covariance

(a) (b)
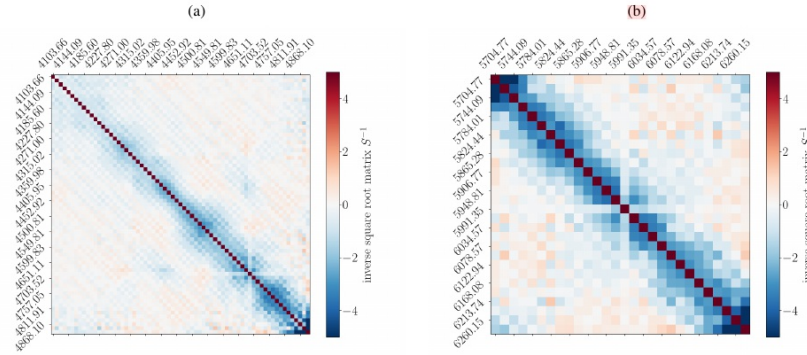
**Figure 6.** Scene 09 background covariance matrix $S$ for the **(a)** 4100-4900 $\mathrm{cm}^{-1}$ (left) and **(b)** 5700-6300 $\mathrm{cm}^{-1}$ (right) spectral range. Note that beside the bad HySpex pixel mentioned in Fig. 2 at 5992.74 $\mathrm{cm}^{-1}$ there appears to be another suspect pixel at 4691.04 $\mathrm{cm}^{-1}$.

#### 2.4.2 Methane enhancement estimate

230 In order to estimate the $CH_4$ plume enhancement light path modifications and the retrieval's vertical sensitivity need to be taken into account. A 'scene average' $CO_2$ scaling factor is used to correct for light path modifications (Frankenberg et al., 2005; Schneising et al., 2009; Krings et al., 2011; Borchardt et al., 2021). In order to apply the $\alpha_{CO2}$ scaling factor to $CH_4$ enhancements for the correction of light path modifications below instrument altitude, the different concentration profiles of $CH_4$ and $CO_2$ (see Fig. 3) need to be taken into account hence $\bar{\alpha}_{CO2}$ is introduced. The 'scene averaging' method was also

235 applied to infer the actual $CH_4$ background profile for the respective overpass. It is important to note that for the $CO_2$ and $CH_4$ background fits ground pixels around the suspected $CH_4$ sources were excluded when computing the average spectrum. The lack of vertical atmospheric resolution in the observed spectrum requires the application of averaging kernels in order to account for the retrieval's altitude sensitivity. The column averaging kernel $\kappa_m(z)$ is used to describe the sensitivity of the total columns to changes in molecular concentrations at different levels (see Buchwitz et al., 2004).

240 The actual $CH_4$ column, which includes corrections for light path modifications via $\bar{\alpha}_{CO2}$ and accounts for the retrieval's vertical sensitivity with respect to the target by $\kappa_{CH4}(z)$, is finally computed as the sum of the background and plume component according to

$$N_{CH4} = N_{bg} + \frac{\alpha_{CH4}}{\bar{\alpha}_{CO2}} \hat{N}_{pl}(z_0) , \qquad (12)$$

statistic, a background statistic $C_i$ is computed for each cluster $i$, determined by k-means clustering (Thorpe et al., 2013; Nesme et al., 2020).

#### 2.4.3 Singular Value Decomposition (SVD)

The retrieval of methane enhancements from hyperspectral AVIRIS data using singular vectors of the observed spectrum plus a
280 target signature was first demonstrated by Thorpe et al. (2014). The SVD method is well-suited for parameter estimation from moderately resolved spectral data because it allows to consider only the most significant components of the spectrum while preserving the main spectral information.

In this study the orthogonal singular vectors are obtained from HySpex spectra that are not impacted by the plume. The scene's log-space background spectra $I_{bg}$ was decomposed into $USV^T$. The target spectrum is represented by the $CH_4$ plume's
285 optical depth $\tau$ which was computed with Py4CAtS.

The basic idea is analogous to the MF, i.e., to represent the general variability in spectral radiance by a linear combination of singular vectors and a target signal. The minimization problem is then given by

$$\min_{w} ||y - Aw||^2 \quad \text{with} \quad Aw = \sum_{k}^{N} u_k w_k + t w_{CH4} \qquad (17)$$

where $A$ represents the concatenated matrix of the first $N$ columns of the unitary matrix $U$. The vector $w$ contains the corre-
290 sponding weights with $\alpha = w_{CH4}$ scaling the contribution of enhanced methane in the lowest atmospheric layers $t = \tau$. In the cluster-tuned variant the background spectra are clustered by k-means and the SVD performed for each cluster separately and the respective base vectors per cluster were then used in the linear fit.

(a) (b)
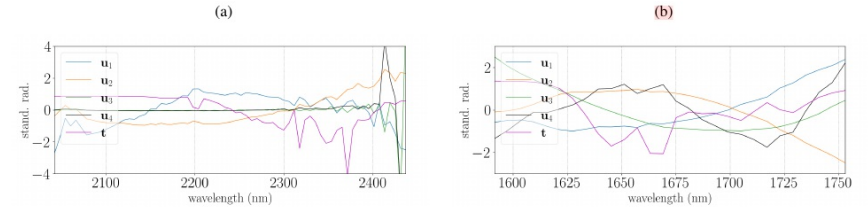
**Figure 5.** Standardized singular vectors and the methane plume's target signature $t$ in 4K (left) and 6K (right) spectral intervals, respectively. Standardization removes the mean and scales to unit variance. While the $u$ vectors were yielded from the SVD the vector $t$ was computed with the radiative transfer model Py4CAtS. Modelling the plume's optical depth with the same tools and for an equivalent setup ($< 2$ km) is crucial for comparability with the nonlinear BIRRA setups.

with

$$\hat{N}_{\mathrm{pl}}(z_0) = \int_{z_0}^{z_{\mathrm{pl}}} \frac{n_{\mathrm{pl}}(z)}{\kappa_{\mathrm{CH4}}(z)}\, \mathrm{d}z \,. \tag{13}$$

The (highly variable) water vapor concentration is co-retrieved with the $CH_4$ plume enhancements as results indicate degeneracy between $H_2O$ and the reflectivity polynomial so that the $H_2O$ scaling factor and reflectivity coefficients need to be interpreted as 'effective' parameters that capture low frequency components in the spectrum. The 'mixing' of usually clearly separated spectral features is attributed to the coarse spectral resolution of HySpex measurements and the fact that water vapor absorption lines of similar strength are distributed over a wide spectral range.

## 2.5 Linear fitting algorithms

### Linear least squares (LLS)

Linearization of the BIRRA forward model with respect to $\alpha_{CH_4}$ allows to infer methane enhancements by linear least squares. In analogy to Thompson et al. (2015, Sec. 2.4) where the $CH_4$ enhancement is estimated from the linear scaling of a target signature that perturbs the mean radiance, linearization of Beer's law caused by an increase in methane's total optical depth in the lowest part of the atmosphere ($< 2\,\mathrm{km}$) with respect to the (saturated, see Thompson et al. (2015)) background concentration is justified.

In order to estimate the unknown parameters in $\boldsymbol{x}$ by linear least squares the power-series expansion for the exponential function $\exp(\tau) := \sum_{n=0}^{\infty} \frac{\tau^n}{n!}$ is exploited. Assuming that the increased optical depth caused by the plume $\tau_{\mathrm{plume}}$ is rather small the Taylor expanded transmission spectrum for the plume can be approximated as

$$\exp\left(-\tau_{\mathrm{plume}}^{\downarrow\uparrow}(\nu)\right) \approx \left(1 - \beta_{\mathrm{CH4}}\, \tau_{\mathrm{plume}}^{\downarrow\uparrow}(\nu)\right)\,. \tag{14}$$

The forward model for the linear least squares problem of $M$ measurements can then be formulated according to

$$\{\boldsymbol{\Phi}(\boldsymbol{x})\}_i = \sum_{j=1}^{N} x_j\, \phi_j(\nu_i), \qquad i = 1, 2, \cdots, M \tag{15}$$

so that the model functions for the linear parameters of the state vector $\boldsymbol{x} = (r_0, b_0 = r_0\,\beta_{CH4})$ are given by

$$\phi_1 = \frac{\cos(\theta)}{\pi} I_{\mathrm{sun}} \mathcal{T}^{\downarrow\uparrow} \otimes S,$$

$$\phi_2 = -\frac{\cos(\theta)}{\pi} I_{\mathrm{sun}} \mathcal{T}^{\downarrow\uparrow} \tau_{\mathrm{plume}}^{\downarrow\uparrow} \otimes S.$$

Note that the reflectivity coefficient $r_0$ is present in both elements of $\boldsymbol{x}$. However, this should not pose a problem for the linear fit as the model functions are different. A brief analysis on the condition of $\boldsymbol{\Phi}(\boldsymbol{x})$ in the 5700–6300 $\mathrm{cm}^{-1}$ interval revealed a condition number is 885. When the higher order reflectivity coefficient $r_1$ is included the number increases by one order of magnitude and another order if $r_2$ added. Therefore, in the current setup, the linear fit is only feasible for the estimate of $r_0$ and $\beta_{CH4}$ at the same time. However, using standardized radiances by dividing by a fitted polynomial eliminates the need for higher order reflectivity coefficients even for large intervals.

### 2.4.4 Spectral signature detection (SSD)

A straightforward approach for detecting spectral methane absorption is the SSD fit which compares the ratio of spectral residual norms to produce a score. Unlike other methods, this approach does not require any radiative transfer calculations, look-up tables, or initial guess information, only calibrated sensor data for a specific interval.

The algorithm is based on a simple polynomial fit of spectral pixels and the calculation of spectral residuals. The idea behind this method is similar to the continuum interpolated band ratio (CIBR) from Green et al. (1989) and Thompson et al. (2015, Eq. 2), which also measure absorption depths (Pandya et al., 2021). The method splits the spectral interval into pixels where $CH_4$ absorbs and where it does not (or only weakly, also see the LLS method) and by linear least squares a polynomial of degree $P$ is fitted to the $M$ out-of-band pixels

$$\min_{\boldsymbol{x}} \|\boldsymbol{y} - \boldsymbol{p}(\boldsymbol{x})\|^2 \quad \text{with} \quad p(\boldsymbol{x}, \nu_i) = \sum_{j=0}^{P} \alpha_j\, \nu_i^j, \qquad j = 1, 2, \cdots, P \quad \text{and} \quad i = 1, 2, \cdots, M. \tag{18}$$

Next the residual norms for the in- and out-of-band pixels are computed and the ratio formed $r_{\mathrm{in}}/r_{\mathrm{out}}$ which provides an absorption band depth score for each observation, i. e., the score indicates variations in the $CH_4$ absorption if in- and out-of-band pixels were properly chosen.

The algorithm constitutes a fast detection scheme which can also be applied for real-time detection of enhancements, e. g., determine whether or not a $CH_4$ ventilation shaft is active at the time of instrument overpass. When a zero order polynomial is used for the out-band fit, the method is comparable to the CIBR algorithm. However, by using higher order polynomials, the method can model the surface reflectivity and other interfering species more precisely, especially over larger spectral intervals.

## 3 Results

This section presents the results for the $CH_4$ estimates from various retrieval methods over the Pniovek V shafts. The site was selected since it showed significant methane releases during the times of overpass in flight track 9 (scene 09) and flight track 11 on June 07, 2018 (see Fig. 1). The results presented subsequently focus on measurements from scene 9. Except otherwise stated, the retrievals were performed on $3 \times 3$ pixels averaged spectra in order to increase the signal-to-noise ratio and thereby reduce scattering of the $CH_4$ fits across pixels.

### 3.1 NLS and SLS fits

Figures 6b and 6c show the results of the classical BIRRA NLS fit. The position of the source is indicated by the intersection of the dashed line. The fits reveals a significant enhancement of $CH_4$ in both spectral intervals above and downwind of the ventilation shaft. However, the bias caused by different surface types is opposite in the 4K and 6K intervals, which is worth mentioning. An analogous behavior is observed for the SLS fit although it is more sensitive to variations in the background.

### 2.5.1 Matched Filter (MF)

A well established method to estimate molecular concentration enhancements from hyperspectral sensors is the MF (Theiler and Foy, 2006; Villeneuve et al., 1999; Funk et al., 2001; Thompson et al., 2015). The linear enhancement factor estimate is based on the perturbation of an average (background) radiance spectrum $\mu$ by a known target spectrum $t$ and is formulated according to

$$\beta(y) = \frac{(J-\mu)^T C^{-1}(y-\mu)}{\sqrt{(J-\mu)^T C^{-1}(J-\mu)}}. \tag{16}$$

The method tests an observed vector $y$ against a base vector represented by e. g. the $CH_4$ plume Jacobian $J$ (computed with a radiative transfer model, e. g., Py4CAtS) while accounting for the background covariance $C$. The method also assumes that the measured spectrum can be represented as a linear superposition of the plumes optical depth and the mean radiance $\mu$ according to

$$y \approx I = \mu(1 - \tau_{pl}^{\downarrow\uparrow}\beta). \tag{17}$$

In order to allow for a comparison to the BIRRA setups, the target's signature $\tau_{pl}^{\downarrow\uparrow}$) represents the vector of optical depth for a low level plume ($< 2$ km with 390 ppm $CH_4$) that is scaled by the linear enhancement factor $\beta$ that perturbs the mean radiance. Note that the mean background spectrum $\mu$ and $C$ were computed per scene and the inverse covariance $C^{-1}$ is approximated by decomposing $C$ into eigenvalues and eigenvectors (Thompson et al., 2015, Eq. 6-8).

As pointed out by Guanter et al. (2021) the classical matched filter is relatively sensitive to surface albedo hence also the cluster tuned matched filter (Funk et al., 2001) was examined. Classification of the image reduces the within-class variance which in turn should reduce the albedo sensitivity of $\beta$. So instead of computing a single covariance (background) statistic the cluster tuned matched filter computes background statistics $C_i$ for each cluster $i$ determined by k-means (Thorpe et al., 2013; Nesme et al., 2020). The elbow method (Thorndike, 1953) was employed to estimate the suitable number of clusters for a scene.

### 2.5.2 Singular Value Decomposition (SVD)

The retrieval of methane enhancements from hyperspectral AVIRIS data using singular vectors of the observed spectrum plus a target signature was first demonstrated by Thorpe et al. (2014). In this study the uncorrelated (orthogonal) singular vectors are obtained from HySpex spectra within a scene (flight track) that are (assumed to be) not impacted by the plume. The scene's mean standardized background spectrum was decomposed while the target spectrum represented by the $CH_4$ plume's Jacobian given by

$$t = -\mu \exp(-\tau_{CH4})\tau_{pl} \quad \text{with} \quad \tau_{CH4} = \tau_{bg} + \beta\tau_{pl} \tag{18}$$

was computed with the radiative trasfer code Py4CAtS. Note that $\tau_{bg}$ represents methane's background optical depth for the lowest, plume impacted layers.
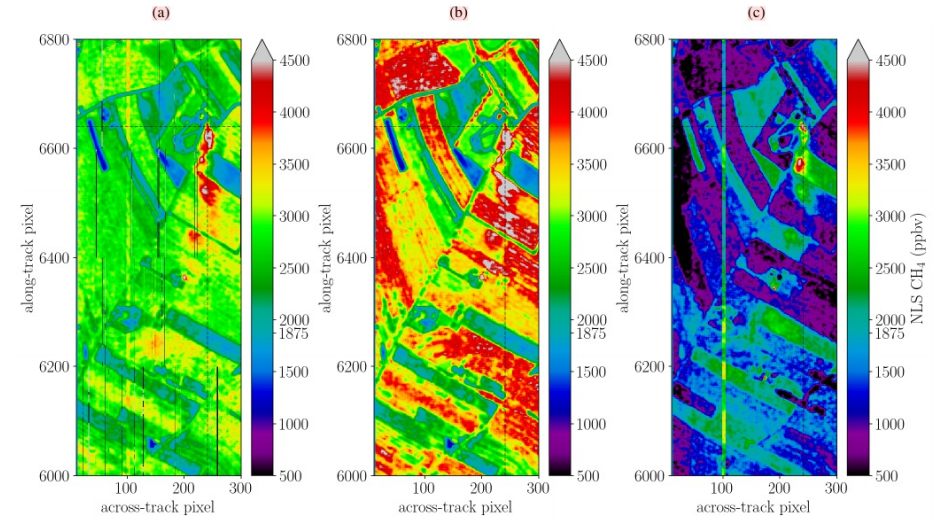
**Figure 6.** Methane enhancements for $3\times3$ spatially averaged HySpex observations in the **(a)** multi-interval fit (combining 4K and 6K ranges). **(b)** shows the result for the 4150–4900 $cm^{-1}$ (4K) interval, while **(c)** depicts enhancements inferred from the 5700–6300 $cm^{-1}$ (6K) range. Note that the latter two fits suffer from albedo correlations with the target in opposite direction.

The multi-interval retrieval shown in Figure 6a improves the result by reducing albedo-induced variabilities on the target, however the retrieval still suffers from surface-correlated offsets but to a much smaller degree than single-interval fits. The maximum enhancements and plume pattern are similar, but the downwind shape of the plume is better captured (see Table 2).

### 3.2 GLS fits

Figure 7 displays the retrieved columns using the generalized least squares (GLS) fit from averaged spectra for scene 09 in the 4K and 6K intervals. Compared to other methods, it reduces the correlation between the methane enhancement and surface reflectivity significantly, resulting in a more distinct plume signal and less background clutter.
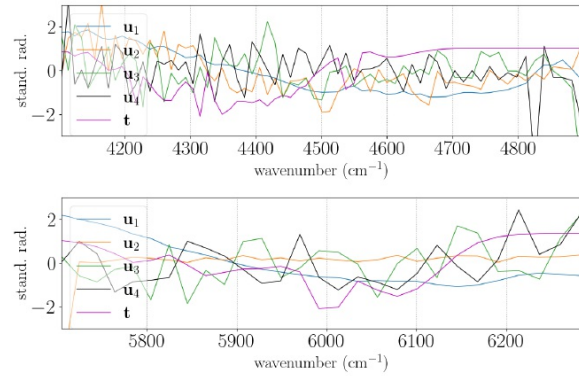
**Figure 7.** The first four singular vectors after standardization, i. e., removing the mean and scaling to unit variance, along with the methane plume's target signature **t**.

The basic idea corresponds to the MF, i. e., to represent the general variability in spectral radiance by a linear combination of singular vectors and a target signal. The minimization problem is then given by

305
$$\min_{\boldsymbol{w}} ||\boldsymbol{y} - \mathsf{A}\boldsymbol{w}||_2^2 \quad \text{with} \tag{19}$$

$$\mathsf{A}\boldsymbol{w} = \sum_{k}^{N} \boldsymbol{u}_k \boldsymbol{w}_k + \boldsymbol{t}\,\boldsymbol{w}_{\text{CH4}} \tag{20}$$

where $\mathsf{A}$ represents the concatenated matrix of the first $N$ columns of the unitary matrix $\mathsf{U}$ and the vector $\boldsymbol{w}$ contains the corresponding weights. The contribution of enhanced methane in the lowest atmospheric layers to the measured radiance is estimated by the corresponding weight of the $CH_4$ target signature.

310    It was found that $N = 4$ is a good choice across spectral intervals as including additional columns significantly increased the condition number of $\mathsf{A}$. It should be noted that cluster tuning was also examined for the SVD fits. In this case the background spectra were clustered by k-means and the SVD performed for each cluster separately and the respective base vectors per cluster were then used in the linear fit.

### 2.5.3 Spectral signature detection (SSD)

315 A very simple yet effective method to detect elevated concentrations of methane in a flight track (subsequently designated as a 'scene') is based on the ratio of spectral residual norms. This method does not require any radiative transfer calculations, look up tables or initial guess information but only calibrated (digital numbers are sufficient) sensor data for a given interval.
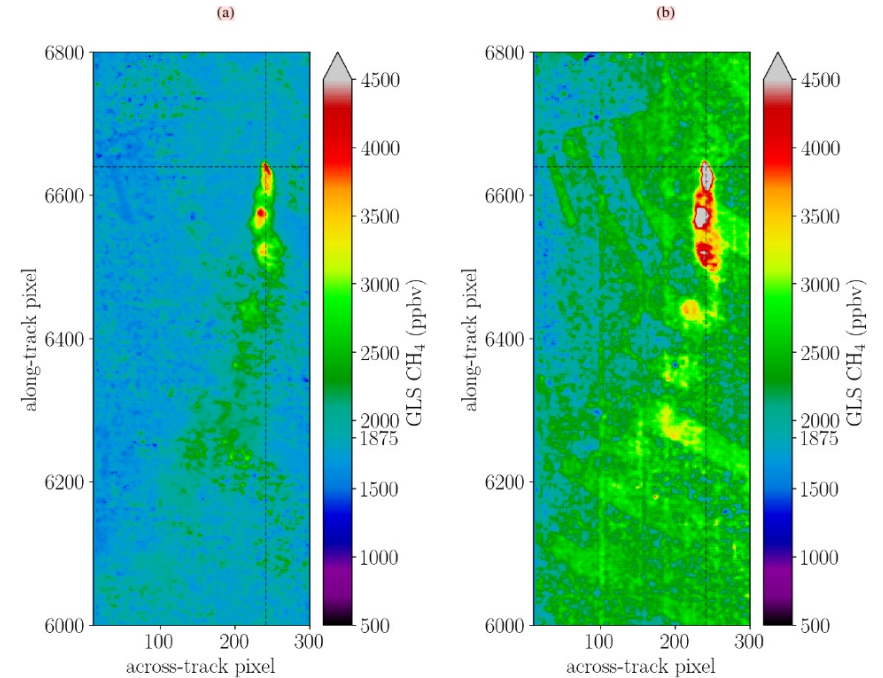
**Figure 7.** Methane plume depicted for the single window covariance weighted fits for scene 09. The background pixel concentration is rather stable in the 4K interval depicted in **(a)** while there is still some overestimation of $CH_4$ in the 6K range in **(b)**.

Figure 8 shows the multi-window covariance weighted GLS fits for scene 09 and 11. In both cases the retrieval yields a distinct plume that separates well from background clutter. Figure 8bshows the impact of decreasing ground pixel resolution
330 (from higher altitudes) on the inferred concentrations as enhancements are less pronounced. However, partly this could also be attributed to less emissions since the observation was taken at another point in time. Also winds could have changed as the plume's shape is different compared to scene 09 in Fig. 8a.

The algorithm is based on a simple polynomial fit of spectral pixels and the computation of spectral residuals. The idea of the method is similar to the continuum interpolated band ratio (CIBR) Green et al. (1989) and Thompson et al. (2015, Eq. 2) which also scores absorption depths (Pandya et al., 2021).

The application of our signature detection method requires the spectral interval including $m$ pixels to be separated into section(s) where $CH_4$ absorbs and where it does not (or only weakly). The detection method then applies a linear least squares to fit a polynomial of some degree $P$ to $Q$ out-band pixels

$$p(\boldsymbol{\beta}, \nu_i) = \sum_{j=0}^{P} \beta_j \nu_i^j, \qquad i = 1, 2, \cdots, Q. \tag{21}$$

Next the residual norms

$$r = ||\boldsymbol{y} - \boldsymbol{p}||_2^2. \tag{22}$$

for the out-band pixels and $(M - Q)$ in-band-pixels are computed so that their ratio

$$s = \frac{r_{\text{in}}}{r_{\text{out}}} \tag{23}$$

yields an absorption band depth score for each observation. Variations in the score indicate variations in the $CH_4$ absorption. If a constant (zero order polynomial) is used for the out-band fit, the method is similar to the CIBR algorithm. With higher order polynomials the wavenumber dependent contributions from the surface reflectivity and other known interfering species could be modeled more accurately, particularly over larger intervals.

The algorithm constitutes a fast detection scheme which can also be applied for real-time detection of enhancements, e. g., determine whether or not a $CH_4$ ventilation shaft is active at the time of instrument overpass.

## 3   Results

In this section the results of the prescribed retrieval methods are presented based on HySpex nadir observations in the short-wave infrared. The section starts with a feasibility study for different BIRRA setups. The results focus on HySpex measurements from flight track 9 (scene 9) since it was found to be the one with the strongest emission at the time of overpass so that the results of the various retrieval schemes can be compared. Note that this ventilation shaft was actually overpassed two times, i. e., in flight tracks 9 and 11 from aircraft altitude $\approx 1520\,\text{m}$ and $\approx 2900\,\text{m}$, respectively. This circumstance could e. g. be used to study the impact of spatial resolution on concentration enhancements.

### 3.1   Beer InfraRed Retrieval Algorithm

The section begins with a feasibility assessment for different BIRRA state vectors and presents the retrieval results from HySpex measurements using the retrieal's NLS, SLS and GLS setups.
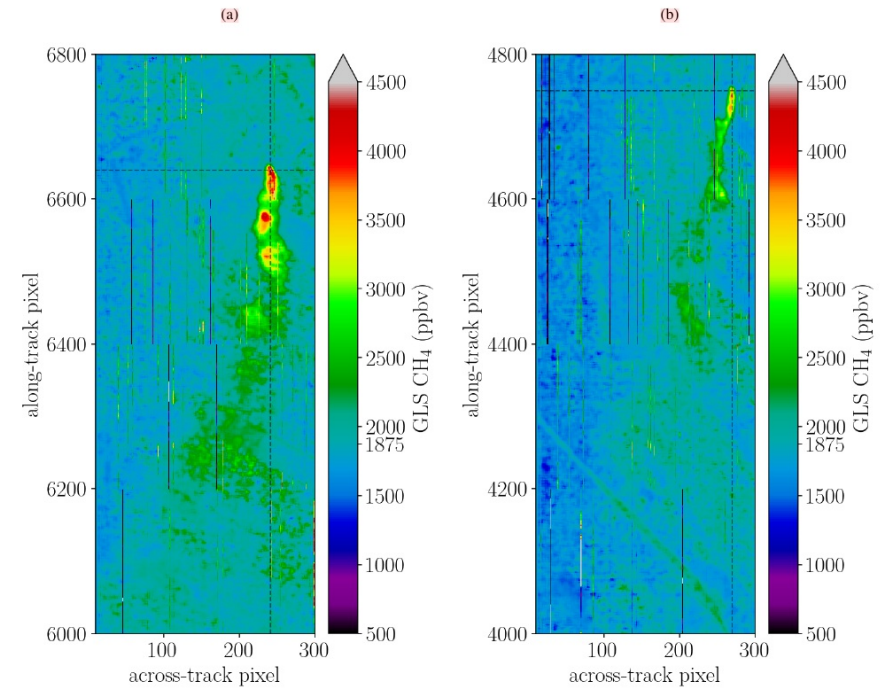
**Figure 8.** Best results are acquired for GLS setups. **(a)** depicts the enhancements for scene 09 while **(b)** depicts the output for scene 11. The stripe pattern in the along track direction is a multi-window retrieval artefact.

Figure 9 depicts the fits from individual (non-averaged) HySpex spectra for scene 09 and 11 for the GLS multi-window retrieval setup. The single pixel total columns are more affected by retrieval noise caused by the lower signal-to-noise ratio (SNR) which varies significantly over different surface-types. However, the method still identifies elevated methane concentrations and is moreover only minor affected by albedo correlations. Also note that the maximum enhancements are more pronounced, particularly in scene 11 where further degrading ground pixel resolution by spatially averaging apparently has somewhat greater impact on downwind concentrations.

### 3.1.1 Feasibility of BIRRA state vectors

According to Table 1 the reduced parameter space in the separated least squares improves the condition number of its Jacobian. The assessment also revealed that increasing the spectral resolution by a factor of two improves the condition number by $\approx 10\,\%$ meaning that the condition number in Fig. 5 would be $\approx 30\,\%$ lower if HySpex would measure at a resolution of $0.2$–$0.3\,\mathrm{cm}^{-1}$ FWHM.

**Table 1.** Condition numbers for the Jacobian matrices of various state vectors of the intervals 4100–4900 $\mathrm{cm}^{-1}$ (designated as 4K) and 5700–6300 $\mathrm{cm}^{-1}$ (6K), respectively. The upper part of the table shows the condition numbers for the nonlinear fit while the lower part gives the conditions for the Jacobians only containing the nonlinear parameters (required for the VarPro solver). The state vector component $N_m = 3$ represent the three molecular scaling factors ($\alpha_{\mathrm{CH4}}$, $\alpha_{\mathrm{H2O}}$, $\alpha_{\mathrm{CO2}}$), $N_a$ stands for the aerosol scaling factors (e. g., $a_1$, $a_2$), and $N_r$ represents the number of coefficients (e. g., $r_0, r_1, r_2$) of the reflectivity polynomial.

| $\boldsymbol{x}$ | 4100–4900 $\mathrm{cm}^{-1}$ (4K) | 5700–6300 $\mathrm{cm}^{-1}$ (6K) | combined |
|---|---|---|---|
| $N_m = 3, N_r = 3, N_a = 0$ | 189 | 1323 | 147 |
| $N_m = 3, N_r = 3, N_a = 1$ | 730 | 2269 | 187 |
| $N_m = 3, N_r = 3, N_a = 2$ | 6681 | 50625 | 198 |
| $\boldsymbol{\eta}$ | 4100–4900 $\mathrm{cm}^{-1}$ (4K) | 5700–6300 $\mathrm{cm}^{-1}$ (6K) | - |
| $N_m = 3$ | 9 | 32 | - |
| $N_m = 3, N_a = 1$ | 47 | 499 | - |
| $N_m = 3, N_a = 2$ | 88 | 839 | - |

### 3.1.2 Nonlinear least squares

The state vector $\boldsymbol{x} = (3m, 3r)$ was found to be robust toward low SNR values across the examined spectral intervals and is hence the first choice for the subsequent retrievals. However, because $CO_2$ is required to account for light path modifications, the actual retrieval fits the state vector $\boldsymbol{x} = (\alpha_{\mathrm{CH4}}, \alpha_{\mathrm{H2O}}, 3r)$. The scene averaged $CO_2$ background level is inferred from the $1.6\,\mu\mathrm{m}$ and/or $2\,\mu\mathrm{m}$ bands via the multi-interval fit. The decision to exclude aerosol parameters from the $CH_4$ plume fit was also encouraged by findings from Borchardt et al. (2021), as they conclude that different aerosol scenarios in the SWIR do not induce errors $> 0.2\,\%$. Moreover, since the spectra are observed at low flight altitudes (between $1500\,\mathrm{m}$ and $3000\,\mathrm{m}$ above mean sea level (MSL)) on a clear day (Luther et al., 2019) retrieval errors induced by aerosol scattering should be negligible in our scenario too (also see Fig. 4) (Thorpe et al., 2013; Thompson et al., 2015). Nonetheless, aerosol extinction according to Eq. (2) could still be included as a given input argument in the forward model.

The $CO_2$ was found to be 385–400 ppm for scene 09 and 365–380 ppm for scene 11 depending on the spectral interval. Given twice the instrument altitude for scene 11 the relative difference of the retrieved values for both scenes is reasonable as changes in $CO_2$ are attributed to light path modifications (light path shortening due to single scattering). The average difference of 20 ppm motivated the choice of a scaling factor $\tilde{\alpha}_{\mathrm{CO2}} = 0.96$ for scene 09 and $\tilde{\alpha}_{\mathrm{CO2}} = 0.93$ for scene 11. The scene averaged
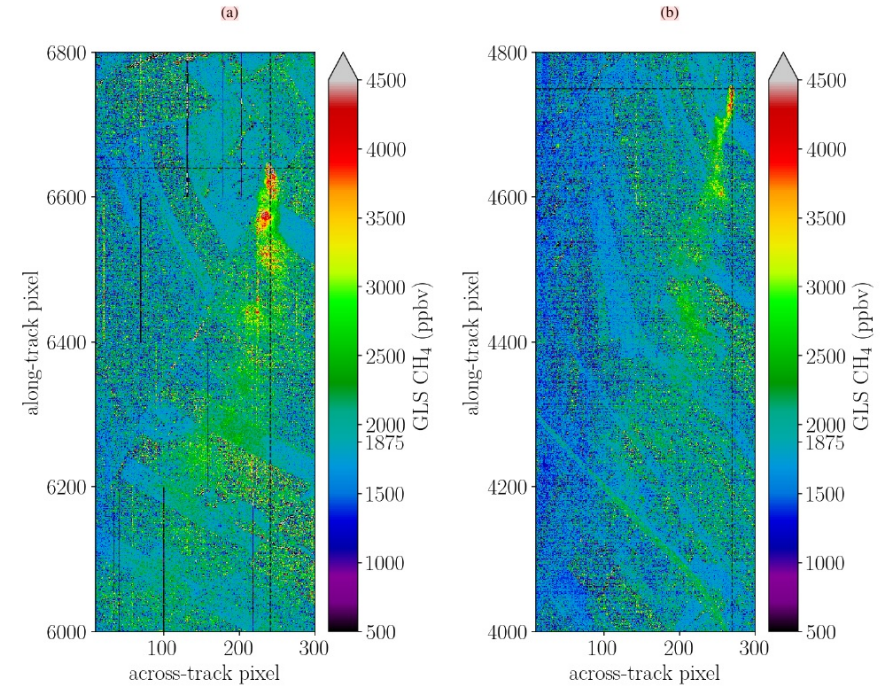
**Figure 9.** Same as Fig. 8 but for single pixel spectra (not $3 \times 3$ averaged). Again **(a)** depicts scene 09 results and **(b)** scene 11.

### 3.3 MF fits

The classical and the albedo normalized matched filter is examined for scene 09. Both variants are able to identify the methane plume but the and as shown in Fig. 10, the cluster-tuning is beneficial in reducing the interference of the plume signal with surface reflectivity.

$CH_4$ background profile was also determined in advance and found to be within 5 % of the initial guess of 1850 ppb so that its

365 initial guess was not scaled.

In Figs. 8a and 8b the results for the retrieval from $3 \times 3$ averaged observations for scene 09 from 4150–4900 $cm^{-1}$ (4K) and 5700–6300 $cm^{-1}$ (6K) are shown, respectively. Averaging over multiple HySpex observations is a way to increase SNR and reduces scattering of the inferred quantities. In both spectral intervals a $CH_4$ enhancement is identified and both reveal significant levels of $CH_4$ (up to ≈4000 ppb) at and close to the source (ventilation shaft). Furthermore, the results agree on

370 the direction of advection. Interestingly the surface-type dependent bias is opposite in the 4K and 6K intervals. The issue of different surfaces types and their impact on the uncertainty of $CH_4$ quantification for moderately resolved spectra was also described by Borchardt et al. (2021) who observed similar features, i. e., paved concrete induces a positive bias while barbed goatgrass leads to large underestimation of enhancements (and so the total column) as at rather coarse spectral resolutions the reflected spectrum shows interfering features similar to the absorption of $CH_4$.
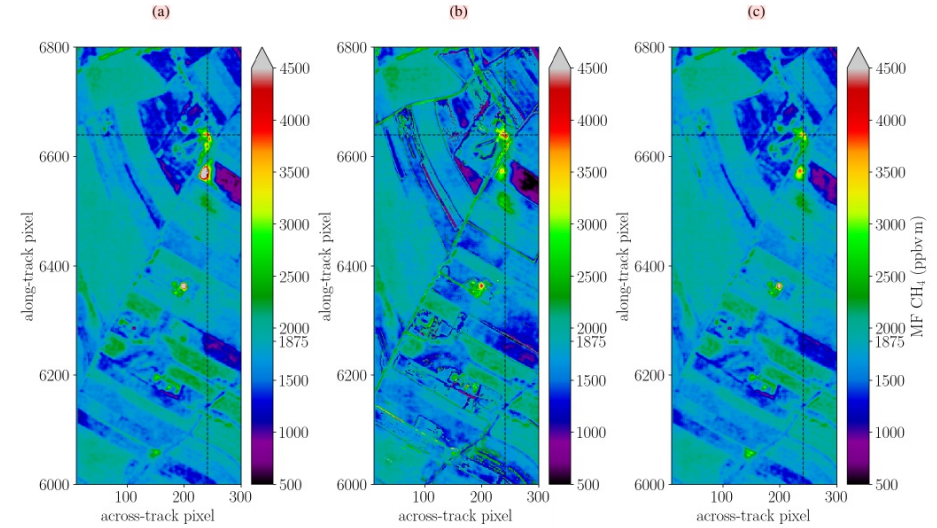
**Figure 10. (a)** Albedo normalized variant of the MF **(b)** the cluster-tuned MF and **(c)** the classical MF fits in the 4K interval (4100-4900 $cm^{-1}$).

### 3.4 SVD fits

The SVD-based retrieval method illustrated in Fig. 11 is able to identifying elevated levels $CH_4$ in the HySpex spectrum.

345 The method yields consistent results for both spectral intervals employing four base vectors and the $CH_4$ Jacobian for lowest 2km (see Fig. 5). Including more than four base vectors significantly increase the condition number of A as columns five interferes with the methane signal. The albedo normalized MF variant yields somewhat larger $CH_4$ values depicted in Fig. 10b compared to the classical variant in Fig. 10c. Cluster-tuning also improves the results in Fig. 10a but since the MF already takes background covariance into account the impact is small.

350 The plume was also identified for the purely 'data-driven' approach, i. e., where the base vector that mimics the $CH_4$ absorption, i. e., the fifth column in U is used instead of the $CH_4$ spectrum. This approach does hence not require any forward model and is hence purely data-driven. Cluster-tuning in general improves the fit due to a reduction in variance within each cluster, however, the results become more sensitive to the selected number of base vectors. It was found that within a cluster the number of base vectors required to ensemble A should be reduced.

(a)       (b)

(c)
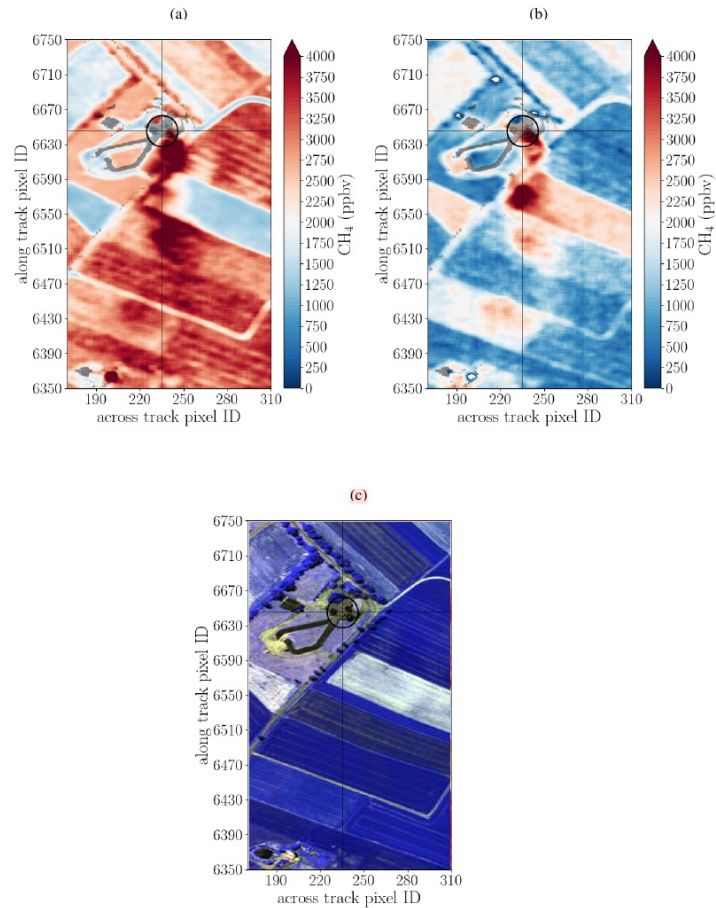
**Figure 8.** Retrieved CH$_4$ enhancement of $3 \times 3$ spatially averaged HySpex observations in the **(a)** 4150–4900 cm$^{-1}$ (4K) range and **(b)** 5700–6300 cm$^{-1}$ (6K) range. Interestingly, the albedo related biases show an almost identical pattern but reverse sign. **(c)** False color image of the SWIR-320m-e camera around the Pniovek V shaft in scene 09.

(a)       (b)
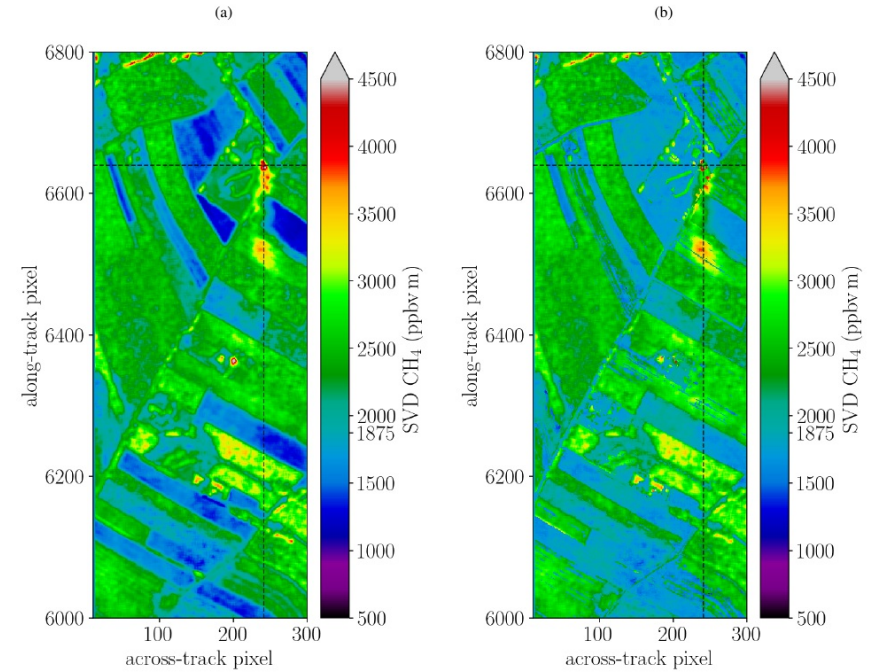
**Figure 11. (a)** Standard SVD fit and **(b)** background cluster-tuned SVD, both for the 6K spectral range. Three clusters reduce background clutter but suppresses some enhancements close to the source. However, also false positives like the spot around the coordinate (200,6350) are diminished.

### 3.5  LLS fits

The results for the linearized BIRRA fits are shown in Fig. 12. The method is able to identify CH$_4$ enhancements, although it differs significantly in the absolute values in the 4K (Fig. 12) and 6K (Fig. 12) spectral range. As pointed out in Sec. 2.4.1, the method is prone to underestimate enhancements. Moreover, the selected weights for the reflectivity coefficients fit were found to impact the CH$_4$ result. However, for the sake of simplicity and since the optimal selection of weights was not clear at the time of writing no weighting was applied. Its CH$_4$ results turned out to be sensitive to which deweight the CH$_4$ impacted pixels. Similar to its nonlinear counterpart (NLS) the fit is also affected by albedo related offsets in opposite directions in the two intervals. However, relative enhancements between plume and background values are rather similar.

375    In spite of a significantly stronger signal in the 6K range (see Fig. 2), the significantly higher condition number of its Jacobians (see Table 5) make both intervals similarly suitable for the retrieval of methane.

With this finding the multi-interval retrieval, i. e., combining 4K and 6K ranges, is expected to yield better results given that methane is fitted across intervals so that the additional constraint alleviates albedo induced variabilities on the target. Figure 9 depicts the inferred $CH_4$ enhancements for scene 09 with the multi-interval retrieval. The surface correlated bias is still present

380    but reduced compared to the single-interval fits. The maximum enhancements and pattern of the $CH_4$ plume is similar but the downwind shape of the plume is better captured.
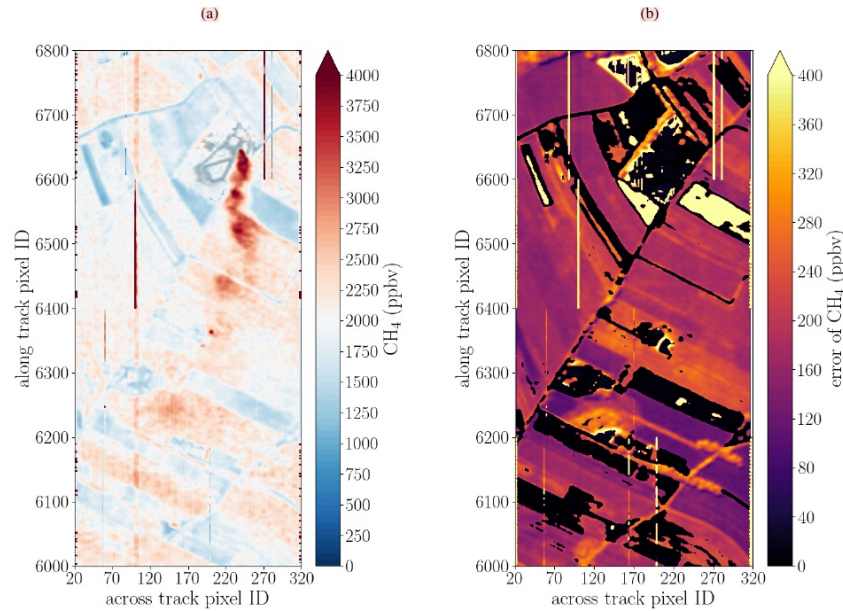
**Figure 9. (a)** Methane plume with corresponding errors in **(b)** inferred for $3 \times 3$ spatially averaged HySpex observations with the multi-interval fit for the combined intervals $4150$–$4900\,\mathrm{cm}^{-1}$ and $5700$–$6300\,\mathrm{cm}^{-1}$. The fitted state vector was $\boldsymbol{x} = (\alpha_{CH4}, \alpha_{H2O}, 6r)$. The bluish colors correlate with either high or very low errors indicating observations with either a small albedo or reflectivity which could not be captured by the second order polynomial.
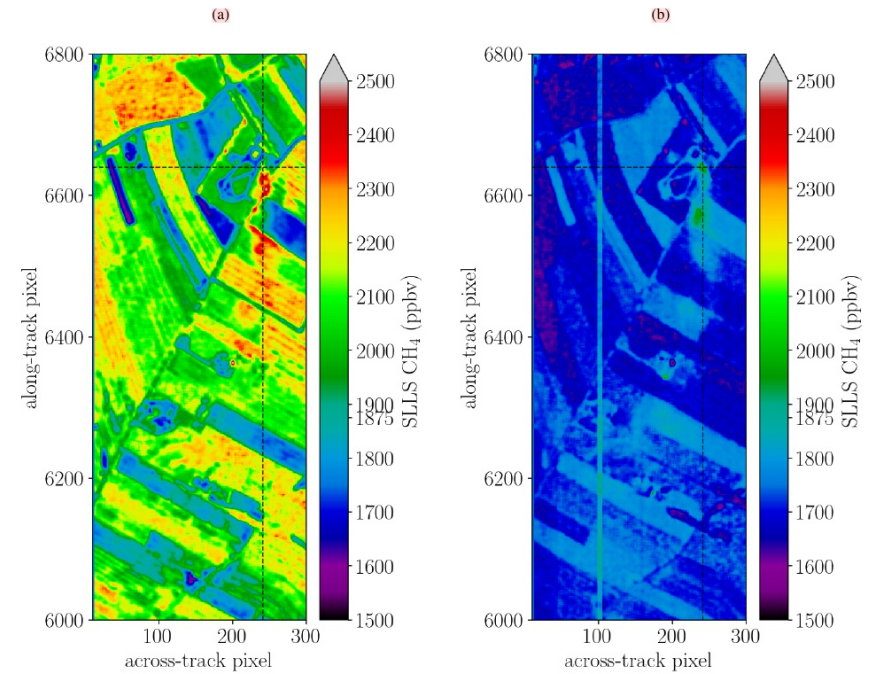
**Figure 12.** $CH_4$ enhancements for scene 09 estimated with the linear forward model setup. The results in Fig. **(a)** show the results for the 4K spectral window while Fig. **(b)** shows 6K outcome. In the latter method, the methane enhancements are less pronounced, but the reflectivity related bias is also smaller.

### 3.6 SSD fits

In Fig. 13 results for the SSD method are shown. A second order polynomial is fitted in Fig. 13a while a constant is used in

365    Fig. 13b. The result show that relative variations are more pronounced in the zero-order fit while the higher order fit better captures the downwind plume by suppressing background clutter.

It is important to note that the method yields better results for the 6K absorption since the 4K absorption features are distributed over a larger spectral range which causes more uncertainty in the out-of-band polynomial fit since many pixels need to be omitted.

In another setup that in addition includes the aerosol parameter $a_1$ similar $CH_4$ concentrations were inferred. However, the $a_1$ estimate adversely affects the fit of the reflectivity coefficients. The impact on $r_0(6K)$ was found to be stronger than on $r_0(4K)$.
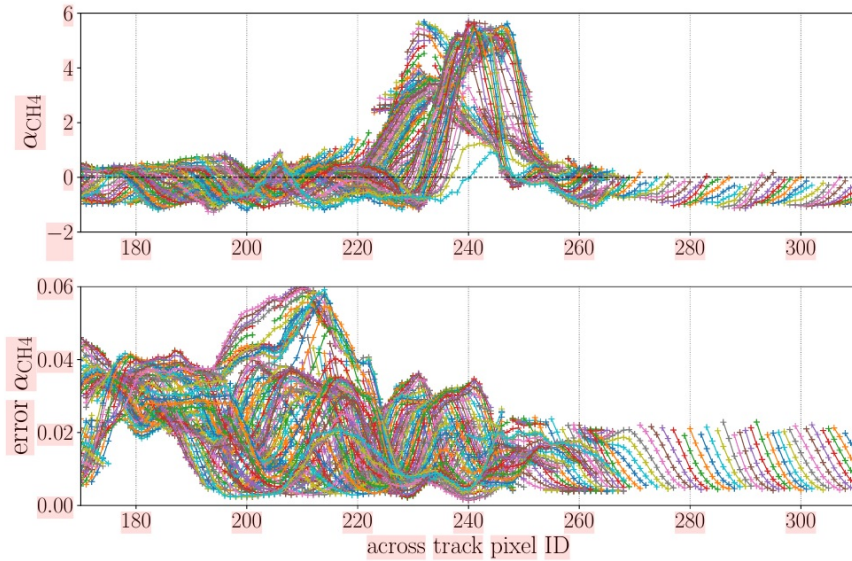
**Figure 10.** Across track depiction of the $3 \times 3$ spatially averaged multi-interval fits from Fig. 9 for the along tracks pixels 6550–6650 are depicted. The top panel shows the corresponding $\alpha_{CH_4}$ scaling factors while the errors are depicted in the lower panel. Note that filtering was applied for this figure.

385     The transverse section of the plume from Fig. 9 between along track pixels 6550–6650 is depicted in Fig. 10. This time the retrieval output was postprocessed so that outliers in the residual norms distribution and reflectivity coefficients $r_0 > 1$ were filtered out. The output clearly identifies stable background $CH_4$ concentrations and a significant enhancement between across track pixels 220–260 (two peaks). Variations in the plume's shape further downwind from the source can also be studied. Note that a almost twofold increase methane's total column corresponds to a $\alpha_{CH_4} \approx 6$ (also see Sec. 3).
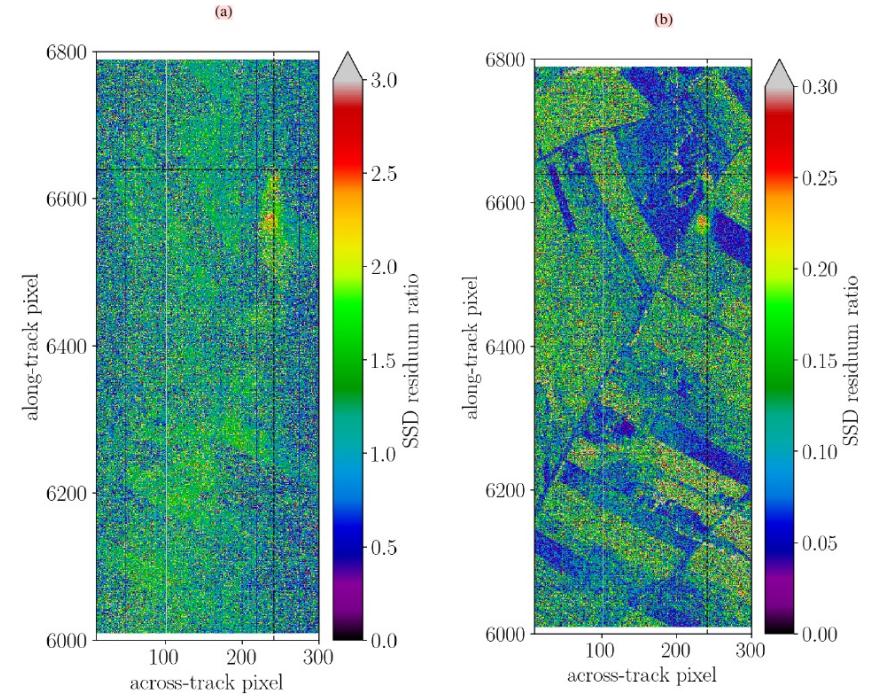
**Figure 13.** The ratio of the spectral residuals in the 6K range for the in- and out-band pixel are depicted. In **(a)** the in-band residuals were computed towards a quadratic polynomial while in **(b)** a constant was used.

370    ### 3.7   Statistical significance of results

In order to provide a more quantitative measure on the quality and confidence of the fits a Student's t-test was applied to the results. The test helps to measure how well the plume is represented with respect to the background for a given retrieval setup. This is accomplished by testing for pixels that contradict the null hypothesis (background pixel) and hence should belong to the plume.

375     The method assumes that the $CH_4$ background samples are normal distributed with equal variance, and that they are independent (Bruce et al., 2020). The null hypothesis was rejected for significance levels 0.01 which can be considered a strong

### 3.1.3 Separable least squares

390

The fit of single HySpex measurements with the separable least squares method turned out to be challenging as many retrievals did not converge due to the rank deficient linear problem. This confirms the findings from our simulations (not shown), which also indicate that the SLS algorithm is more sensitive to the quality of the spectra (SNR). In order to enhance the SNR of the measurements $5 \times 5$ averages were used for the separable fits. The results for the SLS fit (VarPro) for the combined 4K and 6K

395 intervals are depicted in Fig. 11. The retrieval output of the single window 4K and 6K retrieval mimic those of the NLS fit in Fig. 8.
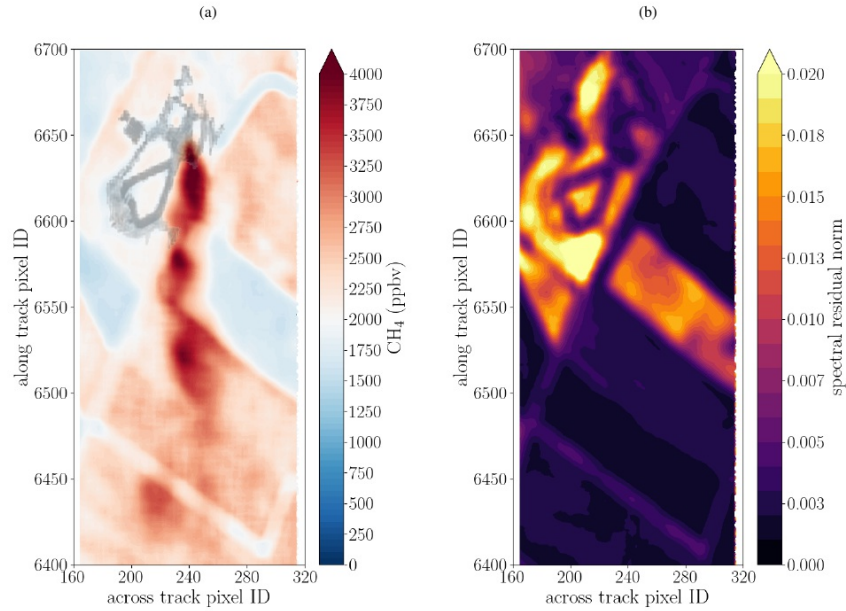
**Figure 11.** SLS fit for the combined 4K and 6K intervals for $5 \times 5$ spatially averaged observations. **(a)** Methane plume enhancement and **(b)** corresponding spectral residual norms.

---

evidence against the null hypothesis. Although some fit results may ask for a tighter significance level in the t-test to isolate the plume and get rid of most outliers, for the sake of comparison 0.01 is used throughout this study.
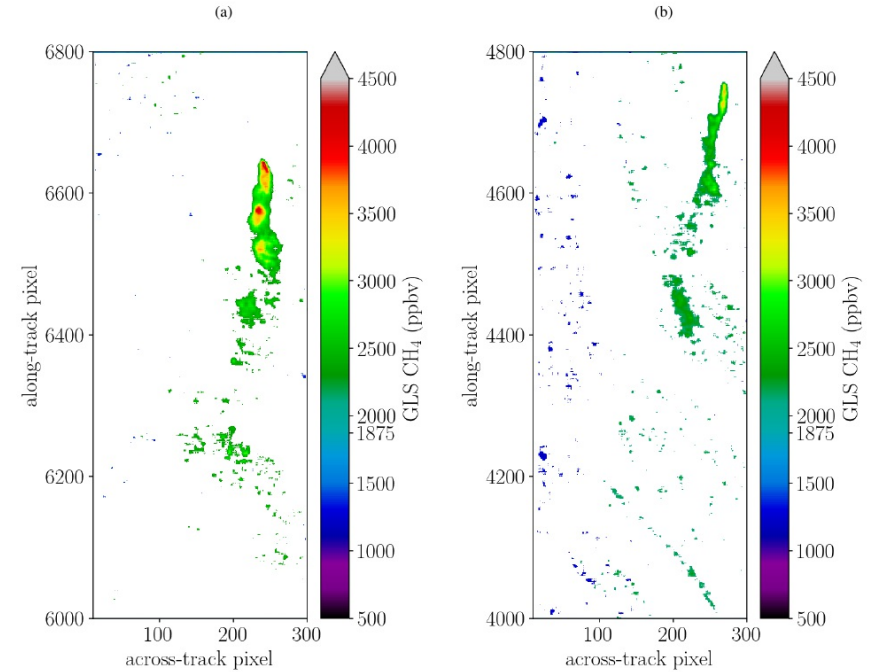
**Figure 14.** Plume pixels according to the Student's t-test for the nonlinear multi-window GLS fit. **(a)** Shows scene 09 while **(b)** displays scene 11.

380 Figure 14 depicts the result of the t-test applied to the retrieval output for scene 09 and 11 from the covariance weighted nonlinear solver (GLS) in the 4K range. The plume is well pronounced and the test is able to isolated enhanced $CH_4$ values from the background. In particular the higher ground-resolution scene 09 shows almost no outliers at the selected significance level meaning that the depicted values occur only in $\leq 1\%$ of the cases given the null hypothesis (background methane concentrations) is true. Moreover, finding such extreme values by chance in such a pattern is even more likely and hence the result gives confidence that the is is a methane plume originating at the source that is transported downwind.

### 3.1.4 Generalized least squares

In Fig. 12 the retrieved columns for the generalized least squares (GLS) fit from $3 \times 3$ averaged observations for scene 09 for the 4K and 6K intervals are shown, respectively. The algorithm employs the inverse of a scene's covariance structure to account for background statistics in the retrieval (Thorpe et al., 2013; Nesme et al., 2020) and is well suited for detecting concentrated sources. Correlation of methane enhancement and surface reflectivity is reduced yielding a more pronounced plume signal.
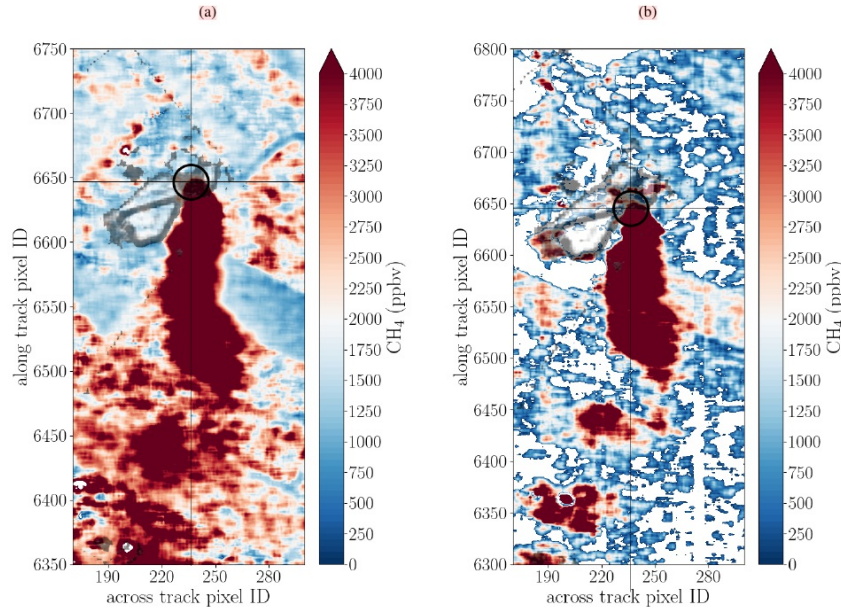
**Figure 12.** Methane plume for the GLS fit from **(a)** 4150–4900 cm$^{-1}$ and **(b)** 5700–6300 cm$^{-1}$ inferred for $3 \times 3$ spatially averaged HySpex observations. White pixels did not converge and are therefore not included in the colorbar. The fitted state vector was $\boldsymbol{x} = (\alpha_{\mathrm{CH4}}, 3r)$.

### 3.1.5 LLS

Methane concentration enhancements can be inferred with the linear retrieval scheme given the state vector and retrieval interval are properly chosen. In Fig. 13a a small retrieval interval of $\pm 50\,\mathrm{cm}^{-1}$ around $6000\,\mathrm{cm}^{-1}$ with the state vector $x =$
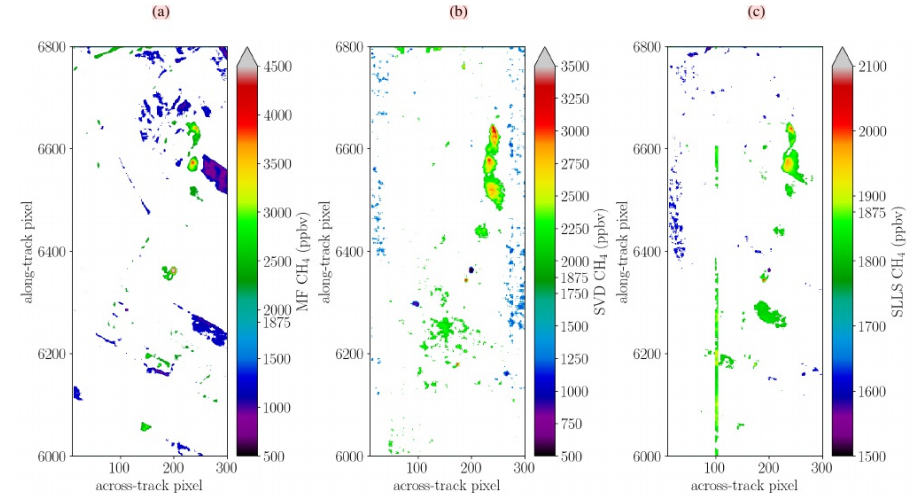
**Figure 15.** Plume pixels identified by the t-test in scene 09 for the different linear schemes. Note that the color scale was adapted. **(a)** Classical MF output from the 4K range, **(b)** displays plume pixels accoding to the SVD method in the 6K interval, and **(c)** presents the SLLS fit in 6K.

The Student's t-test was also applied to the linear solvers and the results are shown in Fig. 15. The test was performed with the same significance levels as above. Each of the linear methods provide enough pixels within the confident range to isolate the plume pixels. While MF provides most accurate enhancement values with respect to the nonlinear solver in Fig 14 the SVD better captures the downwind plume, however, peak enhancements are $\approx 30\,\%$ lower. The LLS method does capture the downwind plume but is much less sensitive to enhancement as it significantly underestimates these.

### 3.8 Errors and correlations

In general the retrieval's fit quality is assessed with respect to the discrepancy between the measurement $\boldsymbol{y}$ and the converged spectrum $\boldsymbol{I}$ according to $\sigma = ||\boldsymbol{y} - \boldsymbol{I}(\hat{\boldsymbol{x}})||$, also known as the residual norm. In order to get the uncertainties (variance) in the estimates of the model parameters for a particular fit, the residual norm is multiplied by the retrieval error covariance matrix

$$\boldsymbol{V} = \frac{\sigma^2}{M-N}\,(\mathsf{J}^{\mathsf{T}}\,\mathsf{J})^{-1} \quad \text{with} \quad \hat{\boldsymbol{x}}_i \pm \sqrt{\boldsymbol{V_{ii}}}\,, \tag{19}$$

representing the standard error for the fitted state vector $\hat{\boldsymbol{x}}$ and J the Jacobi matrix.

405 $(r_0, b_0)$ was used. The small intervals also make the retrieval rather insensitive to variations in the ground albedo. Note that the actual enhancement factor is found by dividing the first element of $x$ by the second element, i.e. $\beta_{CH_4} = b_0/r_0$ (see Sec. 2.5). This setup was able to locate the source and also the drift of the $CH_4$ plume with the wind is traceable several hundred meters from the source. Also the enhancement factors agreed with the nonlinear fit within 20–50 % although the background concentration appears to be negatively biased when compared with the nonlinear fit. The bias turned out to be sensitive to

410 the width of the spectral range and increased towards larger intervals while the fit quality decreased. Moreover, the fit was only stable for small spectral intervals. More reflectivity coefficients have adverse impact on the fit as the problem becomes very ill-conditioned. Using standardized radiances as pointed out in Sec. 2.5 eliminates the need for higher order reflectivity coefficients in the linear fit and allows for larger spectral fit intervals.
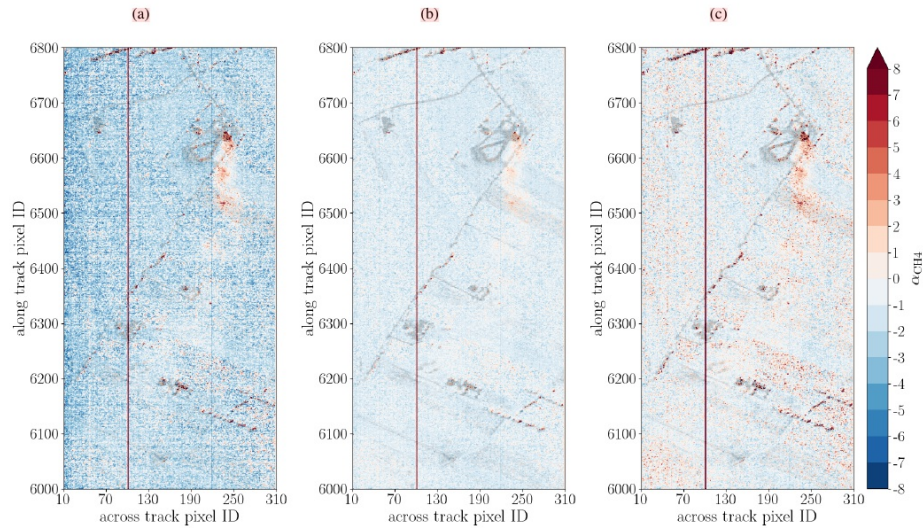
**Figure 13.** Retrieval of $CH_4$ enhancements for individual HySpex observations from scene 09. Results in the first figure **(a)** shows the linear forward model setup with $\boldsymbol{x} = (r_0, b_0)$ from 5930–6080 $cm^{-1}$ while **(b)** shows the subdivision setup $\boldsymbol{x} = (r_0, r1, r2; \beta_{CH4})$ from from 5900–6100 $cm^{-1}$. In the latter method the methane enhancements are less pronounced but the bias is also somewhat smaller. The NLS fit based on Eq. 6 for state vector $\boldsymbol{x} = (r_0, r1, r2, \alpha_{CH4})$ is depicted in **(c)**. Note that the failed retrievals at across pixel ID 104 are caused by the pixel's bad sensitivity at 5992.74 $cm^{-1}$ (see Fig. 2 and 6). It has significant impact on the fit since the selected retrieval interval for the linear fit is small and contains few pixels (see Fig. 2).
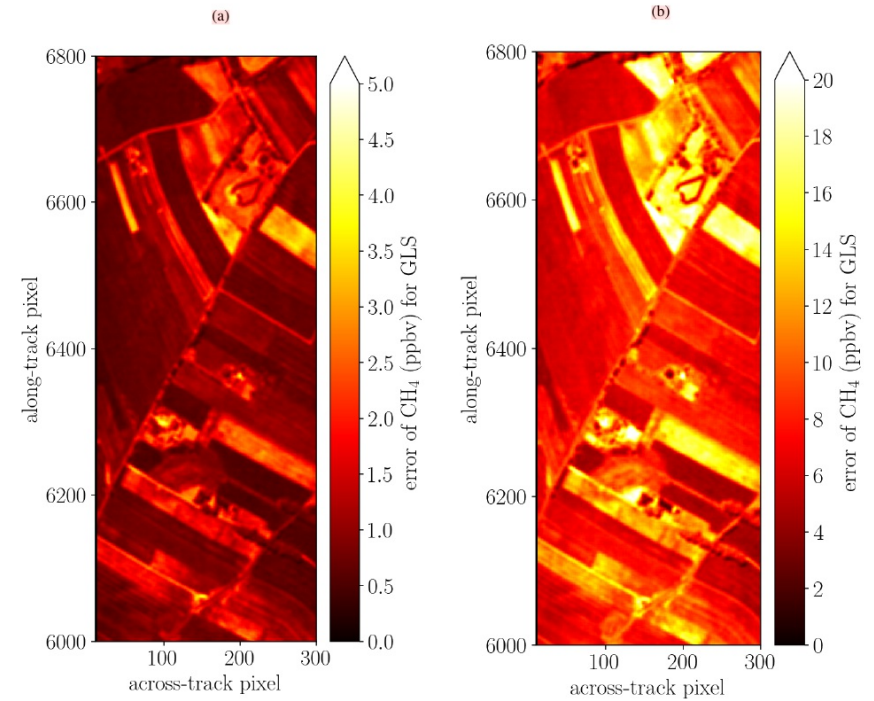
**Figure 16.** Uncertainties in the estimated $CH_4$ according to Eq. 19 for the covariance weighted fit in the **(a)** 4K and **(b)** 6K spectral windows. The 6K range shows larger errors as it contains less than half the number of pixels than the 4K window. Beside the higher variances also the bad pixel close to methane lines depicted in Fig. 2 is also likely to increase the spectral residuum norm.

The errors of the individual state vector parameters are represented in the square root of the diagonal elements of $\boldsymbol{V}$. The standard error $\sqrt{V_{11}}$ for the $CH_4$ scaling factor is shown inf Fig. 16. The uncertainty varies with different surface types which is a product of errors induced by correlation and the spectral residual. A different way to evaluate the quality of the retrieval for a scene is to estimate the fit error from the variability of pixels identified as background by the t-test. This method calculates

400 a score by comparing the means of pixels from the target area and the background area, and dividing this by the standard deviation of the background. These values are also obtainable for all the linear fit variants.

In order to facilitate larger retrieval intervals with higher order reflectivity polynomials a slightly modified linear retrieval setup was examined. It fits the reflectivity coefficients in the 'wings' of the retrieval window and subsequently estimates the enhancement factor $\beta_{CH4}$ in the interval between (the center region of the retrieval window) $x = (r_0, r1, r2; \beta_{CH4})$. The result is shown in Fig. 13b. The setup allows to increase the spectral interval and include additional coefficients in the state vector as the subdivision of the spectral interval avoids the attribution of variations in the $CH_4$ absorption band to the reflectivity polynomial. However, it requires two linear least squares fits, i. e., one to estimate the reflectivity polynomial and another to fit $\beta_{CH4}$. Note that the idea of separating pixels that belong to absorption and not was also employed in the in-band/out-band spectral residual fits in Sec. 2.5.3.

Finally, the 'classical' NLS was applied for the same narrow spectral interval so that its result can be compared to the linear fit. The outcome is depicted in Fig. 13c with the methane source clearly identified. Compared to the linear setup, the nonlinear fits are more sensitive to variations in albedo but yield a smaller bias. The relative enhancement is slightly better represented in Fig. 13a. However, in contrast to the linear fits the NLS fit is able to detect $CH_4$ enhancements for large intervals of several hundred wavenumbers (see Sec. 3.1.2). The analysis also showed that the albedo induced variations in the NLS are less pronounced in scene 11 which was observed at approximately twice the altitude. However, the impact of decreasing ground pixel resolution from higher altitudes on inferred enhancements was also recognized.

### 3.2 Matched Filter

The classical and cluster tuned matched filter was examined for scene 09. Both variants clearly identifies the methane plume, however, as shown in Fig. 14 the cluster tuning is beneficial in reducing the interference of the plume signal with surface reflectivity.

**Table 2.** Mean and standard error for the background pixels of the t-test. Relating the standard error to the mean is a good indication on the accuracy and precision of a method.

| Nonlinear Solvers | Window | Score | Background pixels | |
| --- | --- | --- | --- | --- |
| | | | mean | std. dev. |
| GLS | 4K | 5.34 | 1832 | $\pm$ 150 |
| GLS | 6K | 4.94 | 2051 | $\pm$ 122 |
| GLS | 4K6K | 4.57 | 1926 | $\pm$ 170 |
| SLS | 4K | 3.05 | 3278 | $\pm$ 673 |
| SLS | 6K | 2.22 | 1320 | $\pm$ 537 |
| SLS | 4K6K | 2.94 | 3085 | $\pm$ 577 |
| NLS | 4K | 3.05 | 3247 | $\pm$ 251 |
| NLS | 6K | 2.21 | 1369 | $\pm$ 199 |
| NLS | 4K6K | 3.40 | 2840 | $\pm$ 244 |

Tables 2 and 3 present the findings of this analysis for the nonlinear and linear solvers, respectively. The analysis shows that the GLS fit performs best and that SLS and NLS yield similar results while the MF scores highest amongst the linear solvers. In accordance with Fig. 16 fits in the the 4K window score higher, compared to the 6K. Note that the less sensitive the retrieval is to $CH_4$ enhancements the less variations will be observed in the background. Therefore, the standard deviation in the last column should not be overemphasized in the evaluation of the setups.

**Table 3.** Same as Table 2 but for the linear retrieval setups.

| Linear Solvers | Window | Score | Background pixels | |
| --- | --- | --- | --- | --- |
| | | | mean | std. dev. |
| MF | 4K | 4.22 | 1778 | $\pm$ 208 |
| MF | 6K | 3.20 | 1775 | $\pm$ 217 |
| SVD | 4K | 3.23 | 2237 | $\pm$ 383 |
| SVD | 6K | 3.18 | 1700 | $\pm$ 157 |
| SLLS | 4K | 2.72 | 2069 | $\pm$ 140 |
| SLLS | 6K | 2.71 | 1713 | $\pm$ 145 |

Figure 17 shows the correlation matrix of the retrieval outputs for the various solvers and spectral intervals. It reveals that most solvers have rather good correlations with the GLS solvers (sort of benchmark), particularly in the 4K and 4K6K spectral ranges. Moreover, the GLS, MF and SVD show blocks of high correlation. Blue colors indicate that inferred concentrations tend to move in opposite directions which is the case for example in the single window NLS fits in Fig. 6.
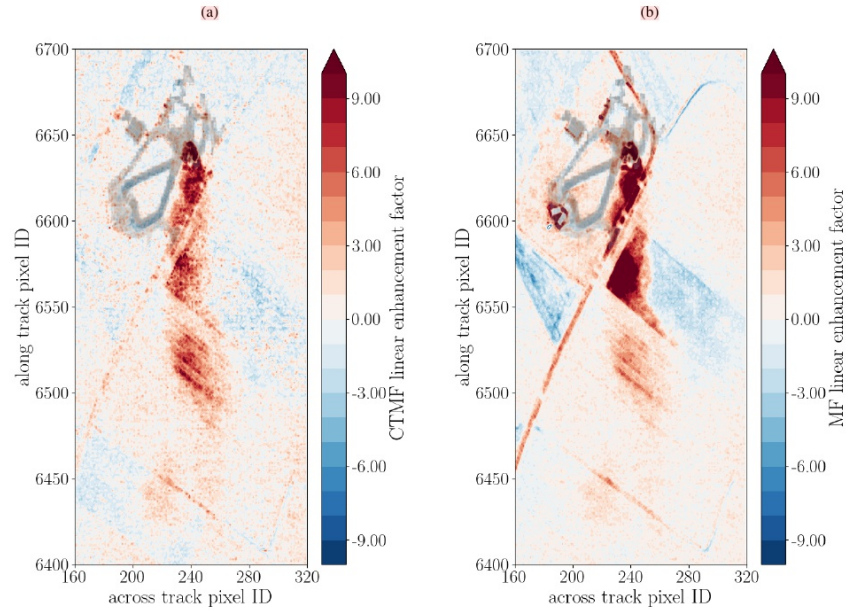
**Figure 14. (a)** Cluster tuned matched filter and **(b)** classical matched filter fits from $4150\text{-}4900\,\mathrm{cm}^{-1}$. The enhancement factor indicates the number of mixing ratio length ($390\,\mathrm{ppm\,m}$) found in the observed spectrum by scaling its Jacobian (see Eq. 16).

### 3.3   Singular Value Decomposition

The retrieval of $CH_4$ via the SVD based method in Fig. 15 can clearly identify the methane plume. The method yields consistent
435   results for both spectral intervals. The retrieval setup employed the first four base vectors and the $CH_4$ Jacobian (see Fig. 7) in the linear least squares fit. Other combinations were tested but higher order base vectors were found to interfere with the methane signal so that this one turned out to give best results when using the $CH_4$ Jacobian from the model output. The plume was also identified for the purely 'data-driven' approach, i. e., where the SVD base vector that mimics the $CH_4$ absorption is used as the target signature (and does not require the forward model's Jacobian).
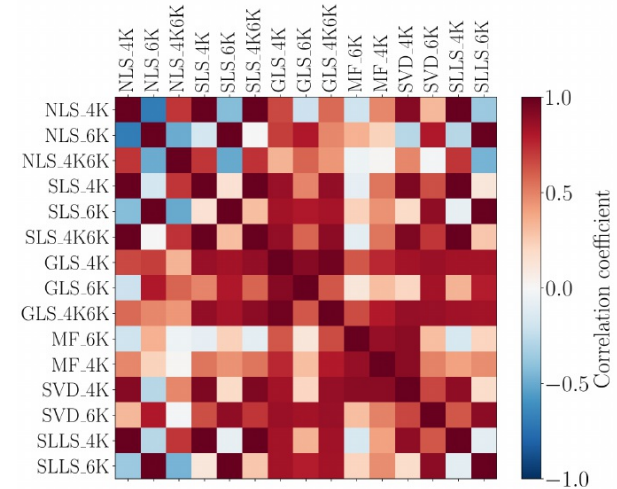
**Figure 17.** Pearson correlation coefficients for inferred methane from scene 09 for the nonlinear and linear solvers in the two examined spectral intervals.

### 4   Discussions

This study found that the BIRRA based nonlinear methods which utilize background pixel covariance statistics (GLS) are able to quantify $CH_4$ concentrations with good accuracy and precision. On the other hand, the unweighted BIRRA suffers from degeneracies between the surface reflectivity and the broad band molecular absorption signal. It was found that the separation
415   of linear (reflectivity coefficients) and nonlinear (target) parameters in the SLS fit does not mitigate the problem of correlation between these quantities but only the inclusion of the background covariance significantly reduces surface reflectance depending biases.

In accordance with Guanter et al. (2021) surface brightness and homogeneity were found to be important factors in detecting and quantifying methane plumes. The issue of different surface types and their impact on the uncertainty of the $CH_4$ enhance-
420   ment was also addressed by Borchardt et al. (2021). In accordance with our results the authors noted that retrieval noise can vary significantly depending on surface type, and that different retrieval schemes can yield disparate total column values (see Fig. 9). For example, they found that paved concrete induces a positive bias while barbed goatgrass leads to a underestimation of enhancements and hence the total columns.

440     It was found that cluster tuning significantly improves the results when only four base vectors plus the model Jacobian are used. The reason is that variance within each cluster is smaller. Moreover, the cluster tuning is beneficial in reducing the interference of the plume signal with surface reflectivity.
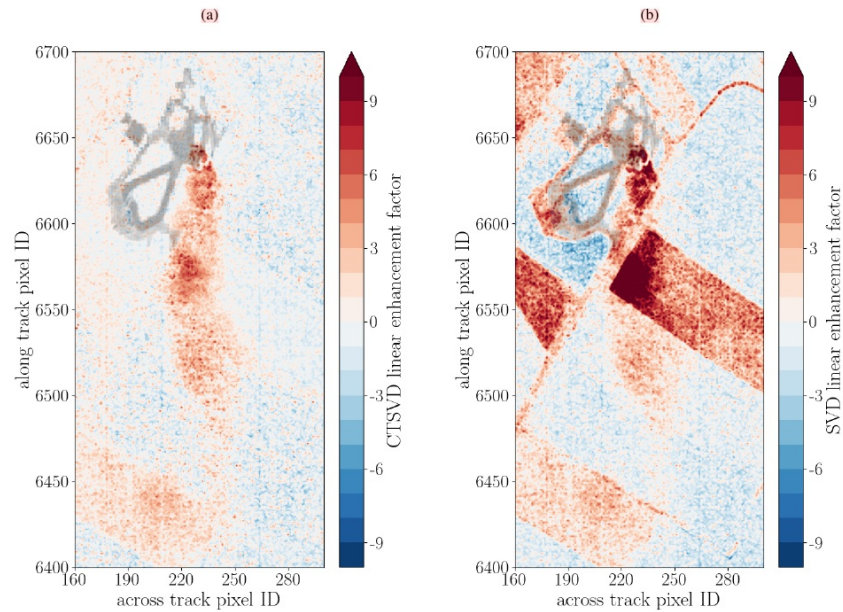
**Figure 15. (a)** Cluster tuned background SVD and **(b)** background SVD fits from $5700\text{-}6300\,\mathrm{cm}^{-1}$. Same as in the MF fit, the enhancement factor indicates the number of reference plumes mixing ratios found in the observed signal. Methane Jacobian was calculated for lowest 2km (the plume component).

### 3.4   SSD

Finally, the SSD method for the detection of enhanced methane concentrations (see Sec. 2.5.3) is assessed. Figure 16 shows
445   the output from Eq. 23 for a zero (a,d,g), first (b,e,h) and second order (c,f,i) polynomial, respectively. The range of the spectral interval upon which the polynomials are fitted vary so that $5960\text{-}6040\,\mathrm{cm}^{-1}$, $5940\text{-}6070\,\mathrm{cm}^{-1}$, and $5920\text{-}6090\,\mathrm{cm}^{-1}$ applies, respectively. The zero order polynomial (a constant—the mean) is rather sensitive to the chosen out-band pixels and only one

In order to scan for potential $CH_4$ leakages on large datasets with millions of pixels, linear solvers such as the SVD, MF or
425   LLS are more appropriate due to their significantly better speed performance. While the iterative setups require roughly one second per fit the linear methods are two, up to three orders of magnitude faster. In particular the SVD and MF solvers yield enhancements that agree well with the more sophisticated nonlinear BIRRA method although their sensitivity and accuracy is lower which in some cases and hampers the ability to detect downwind patterns. Although the SVD method does not explicitly incorporate a covariance matrix it is important to note that the singular vectors are generated from assumed background pixels,
430   hence the solver takes background statistics into account and is considered an equivalent alternative to the MF approach. Both methods are sensitive to the selection of the background and has significant impact on the retrieval result (Thorpe et al., 2014; Foote et al., 2020).

    The simple linearization of the BIRRA forward model lacks background covariance information and hence the fit suffers from albedo correlations similar to its nonlinear counterparts (NLS and SLS). Moreover, the fit significantly underestimates
435   enhancements although it is able to capture parts of the pattern. For the rather simple SSD method polynomials up to second order were able to capture the enhanced methane signal while the selection of an adequate polynomial is depending on the width of the spectral interval and its surface reflectivity. Note that it is not designed to quantify methane but only for (tactical onboard) detection.

    As mentioned by other authors before (e. g. Thompson et al. 2015) linear methods should be regarded as a complement to
440   other more complete retrieval algorithms. While linear methods are well-suited to survey vast datasets and pinpoint potential sources, the iterative BIRRA solvers are adequate to quantify enhanced concentrations at known locations as the slower speed is not of much concern for some thousands of observations.

    Cluster-tuned linear retrieval setups can help to mitigate background clutter and surface reflectivity induced biases (Nesme et al., 2020), however, incorporation of an adequately compiled background covariance matrix into the fitting scheme was
445   found to be more effective. It was also found that allocating the right cluster for the pixel to be retrieved is crucial in order for the method to improve results as otherwise inaccurate background statistics are used for the fit. Nonetheless, cluster-tuning can be a beneficial preprocessing step as it e. g. allows to potentially reduce the base vectors per cluster in the SVD method since background variability is reduced and fewer base vectors are sufficient to model the background spectrum. However, note that in this case a separate model matrix A needs to be compiled for each cluster.

450   ## 5   Conclusions

The study examines the feasibility of methane retrievals from hyperspectral imaging observations using various retrieval methods. It was found that localized $CH_4$ enhancements close to the ground can be quantified from HySpex airborne observations. The generalized covariance weighted BIRRA retrieval is well-suited for investigating potential methane emissions. The statement is underpinned by the relatively low background variations and distinct $CH_4$ enhancement pattern in the surface-albedo
455   covariance weighted BIRRA fits in, e. g., Fig. 8 and Table 2.

or two neighboring out-band pixels should be chosen for the polynomial fit. The higher order fits, in particular the second order, was much less sensitive to the chosen bounds of the interval and yielded enhanced in-band residuals also for larger intervals. Moreover, because the out-band polynomial should capture the reflectivity and (known / not varying) absorption of the interfering molecules (i.e. H2O and $CO_2$) a polynomial up to second order was considered appropriate from the physical perspective. Fig. 16 clearly demonstrated that the second order polynomial is mandatory to capture the surface reflectivity.
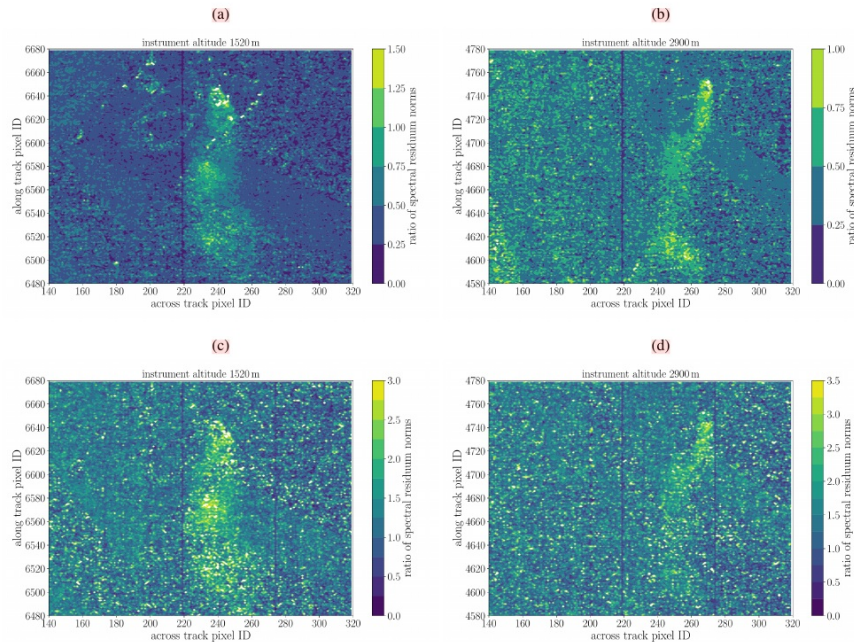
**Figure 16.** The figure depicts results for scene 09 over Pniovek V in the left column and observations from scene 11 from 2.9 km altitude in the right column. The ratio of the spectral residuals for the in- and out-band pixel is depicted. In **(a)** and **(b)** residuals with respect to a mean (a model represented by a constant) from 5960–6040 $cm^{-1}$ are shown while in the second row the fit results for a quadratic polynomial from 5940–6070 $cm^{-1}$ is depicted.

The results show that all three polynomials are able to detect the enhanced $CH_4$ absorption but also indicate that the constant and second order polynomial are best in capturing features from surface reflectivity. In Fig. 16 also the zero and first order

The BIRRA NLS and SLS fits were found to be sensitive to spectral variations in the albedo, leading to surface-type dependent biases that were reported in previous studies utilizing data from hyperspectral sensors. This effect was more pronounced for single spectral intervals but less evident when multiple intervals were used for the fit, such as combining 4K and 6K.

The linear estimators proved to be highly efficient, making them suitable for near real-time processing of large hyperspectral datasets. The well-established MF method for hyperspectral data produced results that agree well with the BIRRA inferred enhancements. The SVD method yields similar enhancements and is able to capture most parts of the downwind plume with great statistical confidence. While also the LLS method is able to capture some of the enhanced plume pixels, it is much less sensitive. For detection purposes the SSD was found to be a useful tool.

In conclusion, covariance weighted methods are able to quantify methane enhancements om hyperspectral SWIR observations at high spatial resolution with good accuracy. The weighted nonlinear methods are more precise and are better suited to capture the downwind plume which is essential for emission estimates. Considering the significant speedup and reasonable accuracy of the linear methods MF and SVD, both constitute a valueable tool in examining plumes on vast datasets.

The methods are applicable to other airborne as well as space borne sensors and this should be considered as a next step. As a final note, the new Python version of the BIRRA code used in this study, based on Py4CAtS as its forward model, turned out to be a flexible toolbox for prototyping.

*Code availability.* Parts of the code are published via the Py4CAtS software suite (see Schreier et al. (2019))

*Data availability.* On request

*Author contributions.* Philipp Hochstaffl (PH) developed and implemented the retrieval setups and analysis tools and wrote the manuscript. Franz Schreier (FS) originally designed and developed the software package Py4CAtS and supported the data evaluation. Claas Köhler (CK) conceived the experimental setup and conducted the data acquisition of the airborne measurements. Andreas Baumgartner (AB) performed the instrument calibration and Level 0-1 processing. CK, AB contributed the experimental setup to the manuscript. Daniele Cerra (DC) gave valuable advice for the cluster-tuning approach and provided spectral unmixing data for the verification of the SVD and MF results. All authors reviewed the manuscript.

*Competing interests.* The authors declare that they have no conflict of interest.

455 polynomial are able to capture most of the surface reflectivity features, although the signal of the plume is relatively weak in the center plots. This result shows that the better the ground resolution (lower flight altitude) the more sensitive the residuals become to albedo variations and the higher the degree of the polynomial should be chosen.

## 4  Discussions

A validation from independent measurements is hence outside the scope of this study and should be examined in a dedicated
460 effort. Although measurements were taken in the Katowice area on June 7th by other instruments, none was made in the very proximity of the shafts (see Luther et al. (2022)). Nonetheless, the results from the well established MF method can be considered some sort of verification. Moreover, the SVD and MF methods were also examined with signatures from independent spectral unmixing algorithms and the results agreed well with $\approx$ 3%. As indicated in Luther et al. (2022, Fig. 4 and 6) wind was present from easterly directions which is in good alignment with the drift of the detected plume (also see Luther et al.
465 (2022, Fig. 4 and 6) and Fig. 1b).

The BIRRA setup utilizing the scenes background pixel (observations not impacted by the methane plume) covariance statistics was found to be the most sensitive method for the detection of enhanced methane, although concentration within the plume is 2-3 times larger than for the classical least squares setup. So for investigating methane emissions at known locations this method is well applicable as its slow speed is not of much concern for some thousands of observations. Howerver, when
470 examining for potential $CH_4$ leakages on large datasets the linear solvers such as the SVD or MF are much more adequate due to their significant better speed performance. Spectral clustering of the background pixels revealed to improve the retrieval results of the linear methods by reducing the correlation of $CH_4$ with surface reflectivity. This is in good agreement with findings by Nesme et al. (2020).

So far only narrow retrieval intervals were used for the linearized BIRRA scheme but with some foreseen modifications a
475 setup that allows for large and even multi interval setups is under investigation.

## 5  Conclusions

The study examines the feasibility of methane retrievals from hyperspectral imaging observations using various retrieval methods. It was found that localized $CH_4$ enhancements close to the ground can be detected and potentially quantified from HySpex airborne observations.
480 The BIRRA NLS fit turned out to be sensitive to spectral variations in the albedo which induced surface-type dependent (positive and negative) biases, an effect that was described by many studies using data from similar hyperspectral sensors (Borchardt et al., 2021). The albedo related correlation was also found in the single retrieval window solutions of the SLS fit, although it splits (separates) the nonlinear from linear (reflectivity) parameters. The effect was dominant for single spectral intervals but less pronounced when multiple intervals were chosen for the fit (e. g. 4K and 6K combined). The multiwindow
485 fits yielded retrieval errors below the maximum encountered enhancements which can be regarded significant. The GLS fit

480 *Acknowledgements.* We thank Thomas Trautmann and Peter Haschberger for valuable criticism of the manuscript. Furthermore we thank Konstantin Gerilowski for initiating coorperation with the CoMet campaign and Andreas Fix as the campaign leader for the support and coordination.

significantly reduced the albedo bias and appears to be less influenced by the underlying surface-type. Moreover, this setup enhances the actual methane signal so that a well pronounced $CH_4$ plume is inferred. The two- to three times higher methane concentrations diminish to a one- or twofold difference when adding the surface related biases in the classical retrieval setups.

The linear estimators turned out to be very fast and hence good for near real time processing of large hyperspectral datasets.
490 The well established MF method for hyperspectral data agree well on the enhancement pattern and confirmed the BIRRA results. The SVD based fit confirmed the results and underlined that the identified enhancement resembles an increased signal of methane absorption. Both linear methods yielded increased performance when the scene was further divided into clusters by applying k-means in a preprocessing step. Another important finding is that both linear methods, SVD and MF, agree well on the plume's shape. It is important to note that the MF yields 50–100 % higher enhancement factors compared to the
495 SVD method which is attributed to the background covariance exploited in the MF method—a behavior also observed in the nonlinear fits.

The linear BIRRA setup was able to detect (and preliminary quantify) $CH_4$ enhancements, particularly in the wavenumber region around $6000\,\mathrm{cm}^{-1}$. However, the linear results are sensitive to the selected combination of spectral interval and state vector. This is also attributed to degeneracies between the surface reflectivity and the broad band molecular absorption features.
500 The linearized forward model also tends to underestimate enhancements which agrees well with findings from Borchardt et al. (2021). In general, narrow retrieval intervals with only one reflectivity coefficient in the state vector turned out to constitute a stable retrieval setup in terms of detecting $CH_4$ enhancements. Nonetheless, it is a very fast retrieval scheme that can process scenes in near real time and simulations (not shown) indicated that the results improve for instruments with higher spectral resolutions so that the linear scheme should definitely be studied for measurements from other sensors.
505 Another simple yet effective method for detecting increased levels of methane is the SSD method. It detects relative enhancements and might serve as a real time (onboard/inflight) analysis tool for uncalibrated spectra. The detection method was able to pinpoint the source over various active shafts. Similar to the linear fit, it yielded best results for small intervals around $6000\,\mathrm{cm}^{-1}$. As pointed out by Thompson et al. (2015) those linear methods should be considered complementary to other more complete retrieval algorithms such as BIRRA.
510 The sensitivity study of retrieval parameters with respect to different SNRs showed that the nonlinear and separable fits rather perform similar for different state vectors. It was shown that low SNRs in the measurement spectrum make the co-retrieval of aerosol optical depth together with a (high order) reflectivity polynomial challenging, rather impossible.

In conclusion, the presented methods are suitable to detect methane enhancements from hyperspectral SWIR observations at high spatial resolution. Moreover, the new Python version of the BIRRA code which uses Py4CAtS as its forward model
515 turned out to be a flexible toolbox for prototyping.

In accordance with Guanter et al. (2021) the brightness and homogeneity of the surface are major drivers for the detection and quantification of methane plumes. Also Borchardt et al. (2021) found that the retrieved total columns suffer from retrieval noise which varies significantly over different surface-types. The study also found large discrepancies in the fitted total columns of two different retrieval algorithms. It also showed that strict filtering might allow to provide enhancement values necessary
520 to calculate fluxes although the absolute concentrations retrieved using the different methods need to be assessed in a separate

## References

Hochstaffl, P.: Trace Gas Concentration Retrieval from Short-Wave Infrared Nadir Sounding Spaceborne Spectrometers, Ph.D. thesis,
485 Ludwig-Maximilians-Universität München, 2022.

Hochstaffl, P., Baumgartner, A., Slijkhuis, S., Lichtenberg, G., Koehler, C. H., Schreier, F., Roiger, A., Feist, D. G., Marshall, J., Butz, A., and Trautmann, T.: CO2Image Retrieval Studies and Performance Analysis, Tech. Rep. EGU23-15635, Copernicus Meetings, https://doi.org/10.5194/egusphere-egu23-15635, 2023.

Rast, M., Nieke, J., Adams, J., Isola, C., and Gascon, F.: Copernicus Hyperspectral Imaging Mission for the Envi-
490 ronment (Chime), in: 2021 IEEE International Geoscience and Remote Sensing Symposium IGARSS, pp. 108–111, https://doi.org/10.1109/IGARSS47720.2021.9553319, 2021.

Duren, R. M., Thorpe, A. K., Foster, K. T., Rafiq, T., Hopkins, F. M., Yadav, V., Bue, B. D., Thompson, D. R., Conley, S., Colombi, N. K., Frankenberg, C., McCubbin, I. B., Eastwood, M. L., Falk, M., Herner, J. D., Croes, B. E., Green, R. O., and Miller, C. E.: California's Methane Super-Emitters, Nature, 575, 180–184, https://doi.org/10.1038/s41586-019-1720-3, 2019.

495 Schreier, F., Gimeno García, S., Milz, M., Kottayil, A., Höpfner, M., von Clarmann, T., and Stiller, G.: Intercomparison of Three Microwave/Infrared High Resolution Line-by-Line Radiative Transfer Codes, in: Radiation Processes in the Atmosphere and Ocean (IRS2012): Proceedings of the International Radiation Symposium (IRC/IAMAS), edited by Cahalan, R. F. and Fischer, J., vol. 1531 of *AIP Conference Proceedings*, pp. 119–122, https://doi.org/10.1063/1.4804722, 2013.

Foote, M. D., Dennison, P. E., Thorpe, A. K., Thompson, D. R., Jongaramrungruang, S., Frankenberg, C., and Joshi, S. C.: Fast and Accurate
500 Retrieval of Methane Concentration From Imaging Spectrometer Data Using Sparsity Prior, IEEE Trans. Geosci. Remote Sens., 58, 6480–6492, https://doi.org/10.1109/TGRS.2020.2976888, 2020.

Ayasse, A. K., Thorpe, A. K., Roberts, D. A., Funk, C. C., Dennison, P. E., Frankenberg, C., Steffke, A., and Aubrey, A. D.: Evaluating the Effects of Surface Properties on Methane Retrievals Using a Synthetic Airborne Visible/Infrared Imaging Spectrometer next Generation (AVIRIS-NG) Image, Remote Sens., 215, 386–397, https://doi.org/10.1016/j.rse.2018.06.018, 2018.

505 Anderson, G., Clough, S., Kneizys, F., Chetwynd, J., and Shettle, E.: AFGL atmospheric constituent profiles (0 - 120 km), Tech. Rep. TR-86-0110, AFGL, 1986.

Baumgartner, A.: Traceable imaging spectrometer calibration and transformation of geometric and spectral pixel properties, Ph.D. thesis, https://doi.org/10.48693/38, 2021.

Baumgartner, A. and Köhler, C. H.: Transformation of point spread functions on an individual pixel scale, Optics Express, 28, 38 682–38 697,
510 https://doi.org/10.1364/oe.409626, tex.date_added: Tue Dec 15 16:52:19 2020, 2020.

Borchardt, J., Gerilowski, K., Krautwurst, S., Bovensmann, H., Thorpe, A. K., Thompson, D. R., Frankenberg, C., Miller, C. E., Duren, R. M., and Burrows, J. P.: Detection and quantification of $CH_4$ plumes using the WFM-DOAS retrieval on AVIRIS-NG hyperspectral data, Atmos. Meas. Tech., 14, 1267–1291, https://doi.org/10.5194/amt-14-1267-2021, 2021.

Bruce, P., Bruce, A., and Gedeck, P.: Practical Statistics for Data Scientists: 50+ Essential Concepts Using R and Python, O'Reilly Media,
515 2020.

Buchwitz, M., Rozanov, V., and Burrows, J.: A near-infrared optimized DOAS method for the fast global retrieval of atmospheric $CH_4$, CO, $CO_2$, $H_2O$, and $N_2O$ total column amounts from SCIAMACHY Envisat-1 nadir radiances, J. Geophys. Res., 105, 15 231–15 245, https://doi.org/10.1029/2000JD900191, 2000.

validation study. Although greenhouse gas observations from HySpex-like sensors are challenging primarily due to its low spectral resolution further studies should investigate the potential for leakage mapping. In a next step, which is outside the scope of this study, the estimation of emission rates should be studied. Furthermore, methods specific to imaging spectrometer data such as spectral unmixing can be tested as an alternative preprocessing steps to cluster the scene for subsequent $CH_4$

525 retrievals based on the MF or SVD as it removes clutter while keeping unaltered the spectral information from the methane plume.

*Code availability.* Parts of the code are published via the Py4CAtS software suite (see Schreier et al. (2019))

*Data availability.* On request

*Author contributions.* Philipp Hochstaffl (PH) developed and implemented the retrieval setups and wrote the manuscript. Franz Schreier

530 (FS) originally designed and developed the software package Py4CAtS and supported the data evaluation. Claas Köhler (CK) conceived the experimental setup and conducted the data acquisition of the airborne measurements. Andreas Baumgartner (AB) performed the instrument calibration and Level 0-1 processing. CK, AB contributed the experimental setup to the manuscript. Daniele Cerra (DC) gave valuable advice for the cluster tuning approach and provided spectral unmixing data for the verification of the SVD and MF results. All authors reviewed the manuscript.

535 *Competing interests.* The authors declare that they have no conflict of interest.

*Acknowledgements.* We thank Thomas Trautmann and Peter Haschberger for valuable criticism of the manuscript. Furthermore we thank Konstantin Gerilowski for initiating coorperation with the CoMet campaign and Andreas Fix as the campaign leader for the support and coordination.

Buchwitz, M., de Beek, R., Bramstedt, K., Noël, S., Bovensmann, H., and Burrows, J. P.: Global carbon monoxide as retrieved from SCIA-
520 MACHY by WFM-DOAS, Atm. Chem. Phys., 4, 1945–1960, https://doi.org/10.5194/acp-4-1945-2004, 2004.

Buchwitz, M., de Beek, R., Noël, S., Burrows, J. P., Bovensmann, H., Bremer, H., Bergamaschi, P., Körner, S., and Heimann, M.: Carbon monoxide, methane and carbon dioxide columns retrieved from SCIAMACHY by WFM-DOAS: year 2003 initial data set, Atm. Chem. Phys., 5, 3313–3329, https://doi.org/10.5194/acp-5-3313-2005, 2005.

Chabrillat, S., Guanter, L., Segl, K., Foerster, S., Fischer, S., Rossner, G., Schickling, A., LaPorta, L., Honold, H.-P., and Storch, T.: The
525 Enmap German Spaceborne Imaging Spectroscopy Mission: Update and Highlights of Recent Preparatory Activities, in: IGARSS 2020 - 2020 IEEE Intern. Geosci. and Remote Sens. Symposium, pp. 3278–3281, https://doi.org/10.1109/IGARSS39084.2020.9324006, 2020.

De Leeuw, G., Kinne, S., Léon, J.-F., Pelon, J., Rosenfeld, D., Schaap, M., Veefkind, P. J., Veihelmann, B., Winker, D. M., and Von Hoyningen-Huene, W.: Retrieval of Aerosol Properties, in: The Remote Sensing of Tropospheric Composition from Space, edited by John P. Burrows, U. P. and Borrell, P., Phys. of Earth and Space Environ., pp. 259–313, Springer-Verlag, https://doi.org/10.1007/978-3-
530 642-14791-3_6, 2011.

Delahaye, T., Armante, R., Scott, N., Jacquinet-Husson, N., Chédin, A., Crépeau, L., Crevoisier, C., Douet, V., Perrin, A., Barbe, A., Boudon, V., Campargue, A., Coudert, L., Ebert, V., Flaud, J.-M., Gamache, R., Jacquemart, D., Jolly, A., Kwabia Tchana, F., Kyuberis, A., Li, G., Lyulin, O., Manceron, L., Mikhailenko, S., Moazzen-Ahmadi, N., Müller, H., Naumenko, O., Nikitin, A., Perevalov, V., Richard, C., Starikova, E., Tashkun, S., Tyuterev, V., Vander Auwera, J., Vispoel, B., Yachmenev, A., and Yurchenko, S.: The 2020 edition of the
535 GEISA spectroscopic database, J. Mol. Spectrosc., 380, 111 510, https://doi.org/https://doi.org/10.1016/j.jms.2021.111510, 2021.

Frankenberg, C., Platt, U., and Wagner, T.: Retrieval of CO from SCIAMACHY onboard ENVISAT: detection of strongly polluted areas and seasonal patterns in global CO abundances, Atm. Chem. Phys., 5, 1639–1644, https://doi.org/10.5194/acp-5-1639-2005, 2005.

Frankenberg, C., Thorpe, A. K., Thompson, D. R., Hulley, G., Kort, E. A., Vance, N., Borchardt, J., Krings, T., Gerilowski, K., Sweeney, C., Conley, S., Bue, B. D., Aubrey, A. D., Hook, S., and Green, R. O.: Airborne Methane Remote Measurements Reveal Heavy-Tail Flux
540 Distribution in Four Corners Region, Proc. Nat. Academy Sciences, 113, 9734–9739, https://doi.org/10.1073/pnas.1605617113, 2016.

Funk, C., Theiler, J., Roberts, D., and Borel, C.: Clustering to improve matched filter detection of weak gas plumes in hyperspectral thermal imagery, IEEE Transactions on Geoscience and Remote Sensing, 39, 1410–1420, https://doi.org/10.1109/36.934073, 2001.

Gerilowski, K., Tretner, A., Krings, T., Buchwitz, M., Bertagnolio, P. P., Belemezov, F., Erzinger, J., Burrows, J. P., and Bovensmann, H.: MAMAP – a new spectrometer system for column-averaged methane and carbon dioxide observations from aircraft: instrument description
545 and performance analysis, Atmos. Meas. Tech., 4, 215–243, https://doi.org/10.5194/amt-4-215-2011, 2011.

Gimeno García, S., Schreier, F., Lichtenberg, G., and Slijkhuis, S.: Near infrared nadir retrieval of vertical column densities: methodology and application to SCIAMACHY, Atmos. Meas. Tech., 4, 2633–2657, https://doi.org/10.5194/amt-4-2633-2011, 2011.

Golub, G. and Pereyra, V.: Separable nonlinear least squares: the variable projection method and its applications, Inverse Problems, 19, R1–R26, https://doi.org/10.1088/0266-5611/19/2/201, 2003.

550 Green, R. O., Carrere, V., and Conel, J. E.: Measurement of atmospheric water vapor using the Airborne Visible/Infrared Imaging Spectrom- eter, in: ASPRS Conference on ImageProcessing, pp. 73–76, 1989.

Green, R. O., Eastwood, M. L., Sarture, C. M., Chrien, T. G., Aronsson, M., Chippendale, B. J., Faust, J. A., Pavri, B. E., Chovit, C. J., Solis, M., Olah, M. R., and Williams, O.: Imaging Spectroscopy and the Airborne Visible/Infrared Imaging Spectrometer (AVIRIS), Remote Sensing of Environment, 65, 227–248, https://doi.org/https://doi.org/10.1016/S0034-4257(98)00064-9, 1998.

## References

540 Anderson, G., Clough, S., Kneizys, F., Chetwynd, J., and Shettle, E.: AFGL atmospheric constituent profiles (0 - 120 km), Tech. Rep. TR-86-0110, AFGL, 1986.

Baumgartner, A.: Traceable imaging spectrometer calibration and transformation of geometric and spectral pixel properties, Ph.D. thesis, https://doi.org/10.48693/38, 2021.

Baumgartner, A. and Köhler, C. H.: Transformation of point spread functions on an individual pixel scale, Optics Express, 28, 38 682–38 697,
545 https://doi.org/10.1364/oe.409626, tex.date_added: Tue Dec 15 16:52:19 2020, 2020.

Borchardt, J., Gerilowski, K., Krautwurst, S., Bovensmann, H., Thorpe, A. K., Thompson, D. R., Frankenberg, C., Miller, C. E., Duren, R. M., and Burrows, J. P.: Detection and quantification of $CH_4$ plumes using the WFM-DOAS retrieval on AVIRIS-NG hyperspectral data, Atmos. Meas. Tech., 14, 1267–1291, https://doi.org/10.5194/amt-14-1267-2021, 2021.

Buchwitz, M., Rozanov, V., and Burrows, J.: A near-infrared optimized DOAS method for the fast global retrieval of atmospheric $CH_4$,
550 CO, $CO_2$, $H_2O$, and $N_2O$ total column amounts from SCIAMACHY Envisat-1 nadir radiances, J. Geophys. Res., 105, 15 231–15 245, https://doi.org/10.1029/2000JD900191, 2000.

Buchwitz, M., de Beek, R., Bramstedt, K., Noël, S., Bovensmann, H., and Burrows, J. P.: Global carbon monoxide as retrieved from SCIA-MACHY by WFM-DOAS, Atm. Chem. Phys., 4, 1945–1960, https://doi.org/10.5194/acp-4-1945-2004, 2004.

Buchwitz, M., de Beek, R., Noël, S., Burrows, J. P., Bovensmann, H., Bremer, H., Bergamaschi, P., Körner, S., and Heimann, M.: Carbon
555 monoxide, methane and carbon dioxide columns retrieved from SCIAMACHY by WFM-DOAS: year 2003 initial data set, Atm. Chem. Phys., 5, 3313–3329, https://doi.org/10.5194/acp-5-3313-2005, 2005.

Chabrillat, S., Guanter, L., Segl, K., Foerster, S., Fischer, S., Rossner, G., Schickling, A., LaPorta, L., Honold, H.-P., and Storch, T.: The Enmap German Spaceborne Imaging Spectroscopy Mission: Update and Highlights of Recent Preparatory Activities, in: IGARSS 2020 - 2020 IEEE Intern. Geosci. and Remote Sens. Symposium, pp. 3278–3281, https://doi.org/10.1109/IGARSS39084.2020.9324006, 2020.

560 De Leeuw, G., Kinne, S., Léon, J.-F., Pelon, J., Rosenfeld, D., Schaap, M., Veefkind, P. J., Veihelmann, B., Winker, D. M., and Von Hoyningen-Huene, W.: Retrieval of Aerosol Properties, in: The Remote Sensing of Tropospheric Composition from Space, edited by John P. Burrows, U. P. and Borrell, P., Phys. of Earth and Space Environ., pp. 259–313, Springer-Verlag, https://doi.org/10.1007/978-3-642-14791-3_6, 2011.

Delahaye, T., Armante, R., Scott, N., Jacquinet-Husson, N., Chédin, A., Crépeau, L., Crevoisier, C., Douet, V., Perrin, A., Barbe, A., Boudon,
565 V., Campargue, A., Coudert, L., Ebert, V., Flaud, J.-M., Gamache, R., Jacquemart, D., Jolly, A., Kwabia Tchana, F., Kyuberis, A., Li, G., Lyulin, O., Manceron, L., Mikhailenko, S., Moazzen-Ahmadi, N., Müller, H., Naumenko, O., Nikitin, A., Perevalov, V., Richard, C., Starikova, E., Tashkun, S., Tyuterev, V., Vander Auwera, J., Vispoel, B., Yachmenev, A., and Yurchenko, S.: The 2020 edition of the GEISA spectroscopic database, J. Mol. Spectrosc., 380, 111 510, https://doi.org/https://doi.org/10.1016/j.jms.2021.111510, 2021.

Frankenberg, C., Platt, U., and Wagner, T.: Retrieval of CO from SCIAMACHY onboard ENVISAT: detection of strongly polluted areas
570 and seasonal patterns in global CO abundances, Atm. Chem. Phys., 5, 1639–1644, https://doi.org/10.5194/acp-5-1639-2005, 2005.

Funk, C., Theiler, J., Roberts, D., and Borel, C.: Clustering to improve matched filter detection of weak gas plumes in hyperspectral thermal imagery, IEEE Transactions on Geoscience and Remote Sensing, 39, 1410–1420, https://doi.org/10.1109/36.934073, 2001.

Gerilowski, K., Tretner, A., Krings, T., Buchwitz, M., Bertagnolio, P. P., Belemezov, F., Erzinger, J., Burrows, J. P., and Bovensmann, H.: MAMAP – a new spectrometer system for column-averaged methane and carbon dioxide observations from aircraft: instrument description
575 and performance analysis, Atmos. Meas. Tech., 4, 215–243, https://doi.org/10.5194/amt-4-215-2011, 2011.

555 Guanter, L., Irakulis-Loitxate, I., Gorroño, J., Sánchez-García, E., Cusworth, D. H., Varon, D. J., Cogliati, S., and Colombo, R.: Mapping methane point emissions with the PRISMA spaceborne imaging spectrometer, Remote Sensing of Environment, 265, 112 671, https://doi.org/https://doi.org/10.1016/j.rse.2021.112671, 2021.

Hansen, P., Pereyra, V., and Scherer, G.: Least Squares Data Fitting with Applications, Johns Hopkins University Press, 2013.

Hochstaffl, P. and Schreier, F.: Impact of Molecular Spectroscopy on Carbon Monoxide Abundances from SCIAMACHY, Remote Sens., 12,
560 1084, https://doi.org/10.3390/rs12071084, 2020.

Hochstaffl, P., Schreier, F., Lichtenberg, G., and Gimeno García, S.: Validation of Carbon Monoxide Total Column Retrievals from SCIA-MACHY Observations with NDACC/TCCON Ground-Based Measurements, Remote Sens., 10, 223, https://doi.org/10.3390/rs10020223, 2018.

Hochstaffl, P., Schreier, F., Birk, M., Wagner, G., Feist, G. D., Notholt, J., Sussmann, R., and Té, Y.: Impact of Molecular Spectroscopy on
565 Carbon Monoxide Abundances from TROPOMI, Remote Sens., 12, 3486, https://doi.org/10.3390/rs12213486, 2020.

Humpage, N., Boesch, H., Palmer, P. I., Vick, A., Parr-Burman, P., Wells, M., Pearson, D., Strachan, J., and Bezawada, N.: GreenHouse gas Observations of the Stratosphere and Troposphere (GHOST): an airborne shortwave-infrared spectrometer for remote sensing of greenhouse gases, Atmos. Meas. Tech., 11, 5199–5222, https://doi.org/10.5194/amt-11-5199-2018, 2018.

(IMF), D. R. S. T. I.: Airborne imaging spectrometer HySpex, Journal of large-scale research facilities, 2, 1–6, https://doi.org/10.17815/jlsrf-
570 2-151, 2016.

Intergovernmental Panel on Climate Change: Climate Change 2013 – The Physical Science Basis: Working Group I Contribution to the Fifth Assessment Report of the Intergovernmental Panel on Climate Change, Cambridge University Press, https://doi.org/10.1017/CBO9781107415324, 2014.

Jervis, D., McKeever, J., Durak, B. O. A., Sloan, J. J., Gains, D., Varon, D. J., Ramier, A., Strupler, M., and Tarrant, E.: The GHGSat-D
575 imaging spectrometer, Atmos. Meas. Tech., 14, 2127–2140, https://doi.org/10.5194/amt-14-2127-2021, 2021.

Kalnay, E., Kanamitsu, M., Kistler, R., Collins, W., Deaven, D., Gandin, L., Iredell, M., Saha, S., White, G., Woollen, J., Zhu, Y., Chelliah, M., Ebisuzaki, W., Higgins, W., Janowiak, J., Mo, K. C., Ropelewski, C., Wang, J., Leetmaa, A., Reynolds, R., Jenne, R., and Joseph, D.: The NCEP/NCAR 40-Year Reanalysis Project, Bull. Am. Met. Soc., 77, 437–472, https://doi.org/10.1175/1520-0477(1996)077<0437:TNYRP>2.0.CO;2, 1996.

580 Krings, T., Gerilowski, K., Buchwitz, M., Reuter, M., Tretner, A., Erzinger, J., Heinze, D., Pflüger, U., Burrows, J. P., and Bovensmann, H.: MAMAP — a new spectrometer system for column-averaged methane and carbon dioxide observations from aircraft: retrieval algorithm and first inversions for point source emission rates, Atmos. Meas. Tech., 4, 1735–1758, https://doi.org/10.5194/amt-4-1735-2011, 2011.

Kuze, A., Suto, H., Nakajima, M., and Hamazaki, T.: Thermal and near infrared sensor for carbon observation Fourier-transform spectrometer on the Greenhouse Gases Observing Satellite for greenhouse gases monitoring, Appl. Opt., 48, 6716–6733,
585 https://doi.org/10.1364/AO.48.006716, 2009.

Kuze, A., Suto, H., Shiomi, K., Kawakami, S., Tanaka, M., Ueda, Y., Deguchi, A., Yoshida, J., Yamamoto, Y., Kataoka, F., Taylor, T. E., and Buijs, H. L.: Update on GOSAT TANSO-FTS performance, operations, and data products after more than 6 years in space, Atmos. Meas. Tech., 9, 2445–2461, https://doi.org/10.5194/amt-9-2445-2016, 2016.

Lauvaux, T., Giron, C., Mazzolini, M., d'Aspremont, A., Duren, R., Cusworth, D., Shindell, D., and Ciais, P.: Global assessment of oil and
590 gas methane ultra-emitters, Science, 375, 557–561, https://doi.org/10.1126/science.abj4351, 2022.

Gimeno García, S., Schreier, F., Lichtenberg, G., and Slijkhuis, S.: Near infrared nadir retrieval of vertical column densities: methodology and application to SCIAMACHY, Atmos. Meas. Tech., 4, 2633–2657, https://doi.org/10.5194/amt-4-2633-2011, 2011.

Golub, G. and Pereyra, V.: Separable nonlinear least squares: the variable projection method and its applications, Inverse Problems, 19, R1–R26, https://doi.org/10.1088/0266-5611/19/2/201, 2003.

580 Green, R. O., Carrere, V., and Conel, J. E.: Measurement of atmospheric water vapor using the Airborne Visible/Infrared Imaging Spectrometer, in: ASPRS Conference on ImageProcessing, pp. 73–76, 1989.

Green, R. O., Eastwood, M. L., Sarture, C. M., Chrien, T. G., Aronsson, M., Chippendale, B. J., Faust, J. A., Pavri, B. E., Chovit, C. J., Solis, M., Olah, M. R., and Williams, O.: Imaging Spectroscopy and the Airborne Visible/Infrared Imaging Spectrometer (AVIRIS), Remote Sensing of Environment, 65, 227–248, https://doi.org/https://doi.org/10.1016/S0034-4257(98)00064-9, 1998.

585 Guanter, L., Irakulis-Loitxate, I., Gorroño, J., Sánchez-García, E., Cusworth, D. H., Varon, D. J., Cogliati, S., and Colombo, R.: Mapping methane point emissions with the PRISMA spaceborne imaging spectrometer, Remote Sensing of Environment, 265, 112 671, https://doi.org/https://doi.org/10.1016/j.rse.2021.112671, 2021.

Hansen, P., Pereyra, V., and Scherer, G.: Least Squares Data Fitting with Applications, Johns Hopkins University Press, 2013.

Hochstaffl, P. and Schreier, F.: Impact of Molecular Spectroscopy on Carbon Monoxide Abundances from SCIAMACHY, Remote Sens., 12, 590 1084, https://doi.org/10.3390/rs12071084, 2020.

Hochstaffl, P., Schreier, F., Lichtenberg, G., and Gimeno García, S.: Validation of Carbon Monoxide Total Column Retrievals from SCIA-MACHY Observations with NDACC/TCCON Ground-Based Measurements, Remote Sens., 10, 223, https://doi.org/10.3390/rs10020223, 2018.

Hochstaffl, P., Schreier, F., Birk, M., Wagner, G., Feist, G. D., Notholt, J., Sussmann, R., and Té, Y.: Impact of Molecular Spectroscopy on 595 Carbon Monoxide Abundances from TROPOMI, Remote Sens., 12, 3486, https://doi.org/10.3390/rs12123486, 2020.

Humpage, N., Boesch, H., Palmer, P. I., Vick, A., Parr-Burman, P., Wells, M., Pearson, D., Strachan, J., and Bezawada, N.: GreenHouse gas Observations of the Stratosphere and Troposphere (GHOST): an airborne shortwave-infrared spectrometer for remote sensing of greenhouse gases, Atmos. Meas. Tech., 11, 5199–5222, https://doi.org/10.5194/amt-11-5199-2018, 2018.

(IMF), D. R. S. T. I.: Airborne imaging spectrometer HySpex, Journal of large-scale research facilities, 2, 1–6, https://doi.org/10.17815/jlsrf-600 2-151, 2016.

Intergovernmental Panel on Climate Change: Climate Change 2013 – The Physical Science Basis: Working Group I Contribution to the Fifth Assessment Report of the Intergovernmental Panel on Climate Change, Cambridge University Press, https://doi.org/10.1017/CBO9781107415324, 2014.

Jervis, D., McKeever, J., Durak, B. O. A., Sloan, J. J., Gains, D., Varon, D. J., Ramier, A., Strupler, M., and Tarrant, E.: The GHGSat-D 605 imaging spectrometer, Atmos. Meas. Tech., 14, 2127–2140, https://doi.org/10.5194/amt-14-2127-2021, 2021.

Kalnay, E., Kanamitsu, M., Kistler, R., Collins, W., Deaven, D., Gandin, L., Iredell, M., Saha, S., White, G., Woollen, J., Zhu, Y., Chelliah, M., Ebisuzaki, W., Higgins, W., Janowiak, J., Mo, K. C., Ropelewski, C., Wang, J., Leetmaa, A., Reynolds, R., Jenne, R., and Joseph, D.: The NCEP/NCAR 40-Year Reanalysis Project, Bull. Am. Met. Soc., 77, 437–472, https://doi.org/10.1175/1520-0477(1996)077<0437:TNYRP>2.0.CO;2, 1996.

610 Krings, T., Gerilowski, K., Buchwitz, M., Reuter, M., Tretner, A., Erzinger, J., Heinze, D., Pflüger, U., Burrows, J. P., and Bovensmann, H.: MAMAP — a new spectrometer system for column-averaged methane and carbon dioxide observations from aircraft: retrieval algorithm and first inversions for point source emission rates, Atmos. Meas. Tech., 4, 1735–1758, https://doi.org/10.5194/amt-4-1735-2011, 2011.

Lenhard, K., Baumgartner, A., and Schwarzmaier, T.: Independent laboratory characterization of neo HySpex imaging spectrometers VNIR-1600 and SWIR-320m-e, IEEE Transactions on Geoscience and Remote Sensing, 53, 1828–1841, https://doi.org/10.1109/tgrs.2014.2349737, tex.date_added: Fri May 24 16:15:14 2019, 2015.

Liou, K.-N.: An Introduction to Atmospheric Radiation, Academic Press, second edn., 2002.

595 Lorente, A., Borsdorff, T., Butz, A., Hasekamp, O., aan de Brugh, J., Schneider, A., Wu, L., Hase, F., Kivi, R., Wunch, D., Pollard, D. F., Shiomi, K., Deutscher, N. M., Velazco, V. A., Roehl, C. M., Wennberg, P. O., Warneke, T., and Landgraf, J.: Methane retrieved from TROPOMI: improvement of the data product and validation of the first 2 years of measurements, Atmos. Meas. Tech., 14, 665–684, https://doi.org/10.5194/amt-14-665-2021, 2021.

Luther, A., Kleinschek, R., Scheidweiler, L., Defratyka, S., Stanisavljevic, M., Forstmaier, A., Dandocsi, A., Wolff, S., Dubravica, D., 600 Wildmann, N., Kostinek, J., Jöckel, P., Nickl, A.-L., Klausner, T., Hase, F., Frey, M., Chen, J., Dietrich, F., Necki, J., Swolkień, J., Fix, A., Roiger, A., and Butz, A.: Towards verifying $CH_4$ emissions from hard coal mines using mobile sun-viewing Fourier transform spectrometry, Atmos. Meas. Tech. Disc., 2019, 1–19, https://doi.org/10.5194/amt-2019-205, 2019.

Luther, A., Kostinek, J., Kleinschek, R., Defratyka, S., Stanisavljević, M., Forstmaier, A., Dandocsi, A., Scheidweiler, L., Dubravica, D., Wildmann, N., Hase, F., Frey, M. M., Chen, J., Dietrich, F., Necki, J., Swolkień, J., Knote, C., Vardag, S. N., Roiger, A., and Butz, 605 A.: Observational constraints on methane emissions from Polish coal mines using a ground-based remote sensing network, Atmospheric Chemistry and Physics, 22, 5859–5876, https://doi.org/10.5194/acp-22-5859-2022, publisher: Copernicus GmbH, 2022.

Masson-Delmotte, V., Zhai, P., Pirani, A., Connors, S., Péan, C., Berger, S., Caud, N., Chen, Y., Goldfarb, L., Gomis, M., Huang, M., Leitzell, K., Lonnoy, E., Matthews, J., Maycock, T., Waterfield, T., Yelekçi, O., Yu, R., and (eds.), B. Z.: Climate Change 2021: The Physical Science Basis. Contribution of Working Group I to the Sixth Assessment Report of the Intergovernmental Panel on Climate 610 Change, Cambridge University Press, https://doi.org/10.1017/CBO9781107415324, 2021.

Nesme, N., Foucher, P.-Y., and Doz, S.: Detection and quantification of industrial methane plume with the airborne Hyspex-NEO camera and applications to satellite data, in: XXIV ISPRS Congress 2020 edition, vol. XLIII-B3-2020, pp. 821 – 827, Online, France, https://doi.org/10.5194/isprs-archives-xliii-b3-2020-821-2020, 2020.

Nickl, A.-L., Mertens, M., Roiger, A., Fix, A., Amediek, A., Fiehn, A., Gerbig, C., Galkowski, M., Kerkweg, A., Klausner, T., Eckl, M., 615 and Jöckel, P.: Hindcasting and forecasting of regional methane from coal mine emissions in the Upper Silesian Coal Basin using the online nested global regional chemistry–climate model MECO(n) (MESSy v2.53), Geoscientific Model Development, 13, 1925–1943, https://doi.org/10.5194/gmd-13-1925-2020, 2020.

OpenStreetMap contributors: Planet dump retrieved from https://planet.osm.org, https://www.openstreetmap.org, 2022.

Pandya, M. R., Chhabra, A., Pathak, V. N., Trivedi, H., and Chauhan, P.: Mapping of thermal power plant emitted atmospheric car-620 bon dioxide concentration using AVIRIS-NG data and atmospheric radiative transfer model simulations, J. Appl. Remote Sens., 15, https://doi.org/10.1117/1.jrs.15.032204, 2021.

Richter, A.: Satellite remote sensing of tropospheric composition - principles, results, and challenges, EPJ Web of Conferences, 9, 181–189, https://doi.org/10.1051/epjconf/201009014, 2010.

Schneising, O., Buchwitz, M., Burrows, J. P., Bovensmann, H., Bergamaschi, P., and Peters, W.: Three years of greenhouse gas column-625 averaged dry air mole fractions retrieved from satellite — Part 2: Methane, Atm. Chem. Phys., 9, 443–465, https://doi.org/10.5194/acp-9-443-2009, 2009.

Kuze, A., Suto, H., Nakajima, M., and Hamazaki, T.: Thermal and near infrared sensor for carbon observation Fourier-transform spectrometer on the Greenhouse Gases Observing Satellite for greenhouse gases monitoring, Appl. Opt., 48, 6716–6733, https://doi.org/10.1364/AO.48.006716, 2009.

Kuze, A., Suto, H., Shiomi, K., Kawakami, S., Tanaka, M., Ueda, Y., Deguchi, A., Yoshida, J., Yamamoto, Y., Kataoka, F., Taylor, T. E., and Buijs, H. L.: Update on GOSAT TANSO-FTS performance, operations, and data products after more than 6 years in space, Atmos. Meas. Tech., 9, 2445–2461, https://doi.org/10.5194/amt-9-2445-2016, 2016.

Lauvaux, T., Giron, C., Mazzolini, M., d'Aspremont, A., Duren, R., Cusworth, D., Shindell, D., and Ciais, P.: Global assessment of oil and gas methane ultra-emitters, Science, 375, 557–561, https://doi.org/10.1126/science.abj4351, 2022.

Lenhard, K., Baumgartner, A., and Schwarzmaier, T.: Independent laboratory characterization of neo HySpex imaging spectrometers VNIR-1600 and SWIR-320m-e, IEEE Transactions on Geoscience and Remote Sensing, 53, 1828–1841, https://doi.org/10.1109/tgrs.2014.2349737, tex.date_added: Fri May 24 16:15:14 2019, 2015.

Liou, K.-N.: An Introduction to Atmospheric Radiation, Academic Press, second edn., 2002.

Lorente, A., Borsdorff, T., Butz, A., Hasekamp, O., aan de Brugh, J., Schneider, A., Wu, L., Hase, F., Kivi, R., Wunch, D., Pollard, D. F., Shiomi, K., Deutscher, N. M., Velazco, V. A., Roehl, C. M., Wennberg, P. O., Warneke, T., and Landgraf, J.: Methane retrieved from TROPOMI: improvement of the data product and validation of the first 2 years of measurements, Atmos. Meas. Tech., 14, 665–684, https://doi.org/10.5194/amt-14-665-2021, 2021.

Luther, A., Kleinschek, R., Scheidweiler, L., Defratyka, S., Stanisavljevic, M., Forstmaier, A., Dandocsi, A., Wolff, S., Dubravica, D., Wildmann, N., Kostinek, J., Jöckel, P., Nickl, A.-L., Klausner, T., Hase, F., Frey, M., Chen, J., Dietrich, F., Necki, J., Swolkień, J., Fix, A., Roiger, A., and Butz, A.: Towards verifying CH$_4$ emissions from hard coal mines using mobile sun-viewing Fourier transform spectrometry, Atmos. Meas. Tech. Disc., 2019, 1–19, https://doi.org/10.5194/amt-2019-205, 2019.

Luther, A., Kostinek, J., Kleinschek, R., Defratyka, S., Stanisavljević, M., Forstmaier, A., Dandocsi, A., Scheidweiler, L., Dubravica, D., Wildmann, N., Hase, F., Frey, M. M., Chen, J., Dietrich, F., N?cki, J., Swolkień, J., Knote, C., Vardag, S. N., Roiger, A., and Butz, A.: Observational constraints on methane emissions from Polish coal mines using a ground-based remote sensing network, Atmospheric Chemistry and Physics, 22, 5859–5876, https://doi.org/10.5194/acp-22-5859-2022, publisher: Copernicus GmbH, 2022.

Masson-Delmotte, V., Zhai, P., Pirani, A., Connors, S., Péan, C., Berger, S., Caud, N., Chen, Y., Goldfarb, L., Gomis, M., Huang, M., Leitzell, K., Lonnoy, E., Matthews, J., Maycock, T., Waterfield, T., Yelekçi, O., Yu, R., and (eds.), B. Z.: Climate Change 2021: The Physical Science Basis. Contribution of Working Group I to the Sixth Assessment Report of the Intergovernmental Panel on Climate Change, Cambridge University Press, https://doi.org/10.1017/CBO9781107415324, 2021.

Nesme, N., Foucher, P.-Y., and Doz, S.: Detection and quantification of industrial methane plume with the airborne Hyspex-NEO camera and applications to satellite data, in: XXIV ISPRS Congress 2020 edition, vol. XLIII-B3-2020, pp. 821 – 827, Online, France, https://doi.org/10.5194/isprs-archives-xliii-b3-2020-821-2020, 2020.

Nickl, A.-L., Mertens, M., Roiger, A., Fix, A., Amediek, A., Fiehn, A., Gerbig, C., Galkowski, M., Kerkweg, A., Klausner, T., Eckl, M., and Jöckel, P.: Hindcasting and forecasting of regional methane from coal mine emissions in the Upper Silesian Coal Basin using the online nested global regional chemistry–climate model MECO(n) (MESSy v2.53), Geoscientific Model Development, 13, 1925–1943, https://doi.org/10.5194/gmd-13-1925-2020, 2020.

OpenStreetMap contributors: Planet dump retrieved from https://planet.osm.org, https://www.openstreetmap.org, 2022.

Schreier, F., Gimeno García, S., Hedelt, P., Hess, M., Mendrok, J., Vasquez, M., and Xu, J.: GARLIC – A General Purpose Atmospheric Radiative Transfer Line-by-Line Infrared-Microwave Code: Implementation and Evaluation, J. Quant. Spectrosc. & Radiat. Transfer, 137, 29–50, https://doi.org/10.1016/j.jqsrt.2013.11.018, 2014.

Schreier, F., Gimeno García, S., Hochstaffl, P., and Städt, S.: Py4CAtS — PYthon for Computational ATmospheric Spectroscopy, Atmosphere, 10, 262, https://doi.org/10.3390/atmos10050262, 2019.

Theiler, J. and Foy, B.: Effect of signal contamination in matched-filter detection of the signal on a cluttered background, Geosci. Remote Sens. Letters, 3, 98–102, https://doi.org/10.1109/LGRS.2005.857619, 2006.

Thompson, D. R., Leifer, I., Bovensmann, H., Eastwood, M., Fladeland, M., Frankenberg, C., Gerilowski, K., Green, R. O., Kratwurst, S., Krings, T., Luna, B., and Thorpe, A. K.: Real-time remote detection and measurement for airborne imaging spectroscopy: a case study with methane, Atmos. Meas. Tech., 8, 4383–4397, https://doi.org/10.5194/amt-8-4383-2015, 2015.

Thompson, D. R., Thorpe, A. K., Frankenberg, C., Green, R. O., Duren, R., Guanter, L., Hollstein, A., Middleton, E., Ong, L., and Ungar, S.: Space-based remote imaging spectroscopy of the Aliso Canyon CH4 superemitter, Geophys. Res. Letters, 43, 6571–6578, https://doi.org/https://doi.org/10.1002/2016GL069079, 2016.

Thorndike, R. L.: Who belongs in the family, Psychometrika, pp. 267–276, 1953.

Thorpe, A. K., Roberts, D. A., Bradley, E. S., Funk, C. C., Dennison, P. E., and Leifer, I.: High resolution mapping of methane emissions from marine and terrestrial sources using a Cluster-Tuned Matched Filter technique and imaging spectrometry, Remote Sensing of Environment, 134, 305–318, https://doi.org/10.1016/j.rse.2013.03.018, 2013.

Thorpe, A. K., Frankenberg, C., and Roberts, D. A.: Retrieval techniques for airborne imaging of methane concentrations using high spatial and moderate spectral resolution: application to AVIRIS, Atmos. Meas. Tech., 7, 491–506, https://doi.org/10.5194/amt-7-491-2014, 2014.

United Nations Framework Convention on Climate: Paris Agreement to the United Nations Framework Convention on Climate Change, https://unfccc.int/files/meetings/paris_nov_2015/application/pdf/paris_agreement_english_.pdf, accessed: 2021-04-01, 2015.

Varon, D. J., McKeever, J., Jervis, D., Maasakkers, J. D., Pandey, S., Houweling, S., Aben, I., Scarpelli, T., and Jacob, D. J.: Satellite Discovery of Anomalously Large Methane Point Sources From Oil/Gas Production, Geophys. Res. Letters, 46, 13 507–13 516, https://doi.org/https://doi.org/10.1029/2019GL083798, 2019.

Veefkind, J., Aben, I., McMullan, K., Förster, H., de Vries, J., Otter, G., Claas, J., Eskes, H., de Haan, J., Kleipool, Q., van Weele, M., Hasekamp, O., Hoogeveen, R., Landgraf, J., Snel, R., Tol, P., Ingmann, P., Voors, R., Kruizinga, B., Vink, R., Visser, H., and Levelt, P.: TROPOMI on the ESA Sentinel-5 Precursor: A GMES mission for global observations of the atmospheric composition for climate, air quality and ozone layer applications, Remote Sensing of Environment, 120, 70 – 83, https://doi.org/10.1016/j.rse.2011.09.027, the Sentinel Missions - New Opportunities for Science, 2012.

Villeneuve, P. V., Fry, H. A., Theiler, J. P., Clodius, W. B., Smith, B. W., and Stocker, A. D.: Improved matched-filter detection techniques, in: Imaging Spectrometry V, edited by Descour, M. R. and Shen, S. S., vol. 3753, pp. 278 – 285, International Society for Optics and Photonics, Proc. SPIE, https://doi.org/10.1117/12.366290, 1999.

Zdunkowski, W., Trautmann, T., and Bott, A.: Radiation in the Atmosphere: A Course in Theoretical Meteorology, Cambridge University Press, 2007.